G (Molecular Probes, Eugene, OR). Fluorescence signals were detected with a confocal laser-scanning microscope (LSM 410; Carl Zeiss, Oberkochen, Germany).

3. Results

3.1. Reduction of endogenous TTP mRNA levels increased HIV-1 production

We initially examined whether reduction of endogenous TTP in a latently HIV-1 infected cell line would increase HIV-1 production following stimulation. The U1 cell line is transcriptionally latent in terms of HIV-1 expression, and is activated by treatment with several reagents [21,22]. Under normal culture conditions, less than 5% of the cells continuously express HIV-1 antigens [22]. Stimulation of U1 cells with phorbol 12-myristate 13-acetate (PMA) significantly increased the population of HIV-1 antigen-expressing cells up to 40% at 10 h. At the present time, no antibody capable of detecting human endogenous TTP expression is available (personal communication). Therefore, we examined TTP mRNA levels in U1 cells transfected with TTP siRNA or control siRNA. Following treatment of PMA, TTP mRNA peaked at 4 h in U1 cells transfected with control siRNA (Fig. 1A), as previously reported [23]. In contrast, in U1 cells transfected with TTP siRNA PMA stimulation increased TTP mRNA significantly less than cells transfected with control siRNA. Following 48 h stimulation by PMA, p24 levels in the supernatant in U1 cells transfected with TTP siRNA were found to be increased (Fig. 1B), suggesting that TTP decreases HIV-1 production.

3.2. Suppression of HIV-1 production by exogenous TTP

To determine whether exogenous TTP is able to affect HIV-1 production, we co-expressed human TTP and the HIV-1 clone pNL-Luc-E$^-$R$^+$ [24] in HEK293T cells. The amounts of p24 and genomic RNA in culture supernatants were markedly reduced by TTP (maximal inhibition of 97% and 86%, respectively) in a concentration-dependent manner (Fig. 2A–C).

We investigated the functional domains of TTP responsible for the inhibition of HIV-1 production by co-expressing various TTP mutants (Fig. 2D,E) with pNL-Luc-E$^-$R$^+$ in HEK293T cells. A TTP mutant (1–101) that lacks the COOH-terminal region containing the nuclear localization sequence (NLS) inhibited HIV-1 virion production to an extent similar to that observed with the wild-type protein (Fig. 2F). In contrast, the NH_2-terminal deletion mutants 76–189 and 176–320, both of which lack the nuclear export sequence (NES), did not significantly inhibit HIV-1 production (Fig. 2F). The expression level of TTP mutant (176–320) was much lower than other recombinant wild-type and mutants TTPs (1–101 and 76–189) and this result was also observed when the mutants were subcloned into another plasmid, pcDNA4/HisMax-C used in the Fig. 6, suggesting the amino acid residue (1–175) might play a role in stable

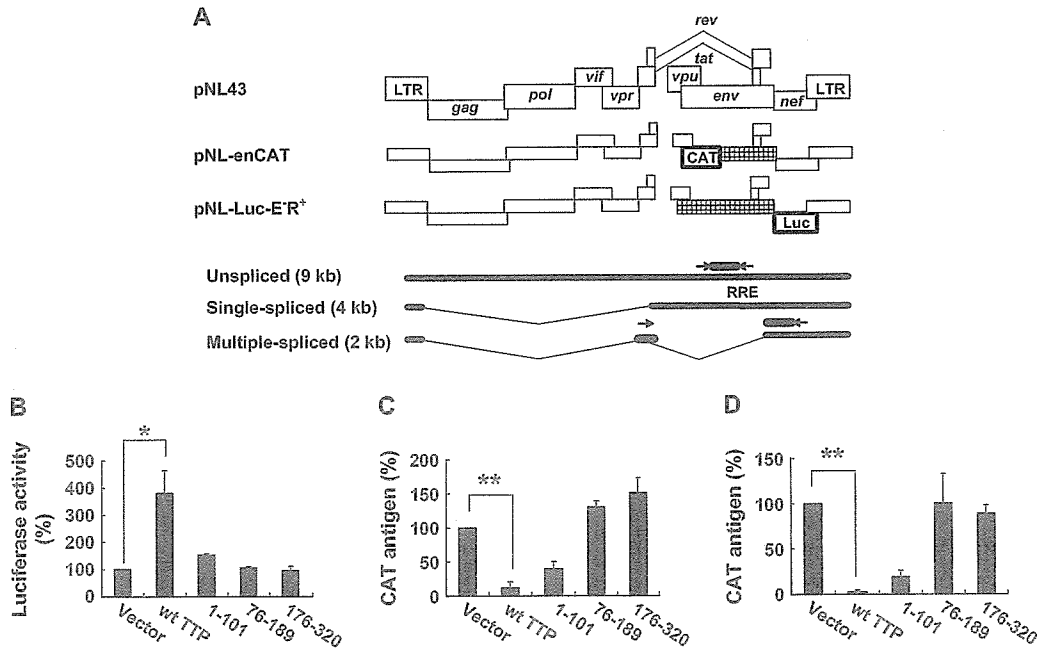

Fig. 3. Promotion of multiple splicing of HIV-1 RNA by TTP. (A) Schematic representations of pNL43, pNL-enCAT, and pNL-Luc-E$^-$R$^+$. The sites of PCR primers and probes for quantitative PCR were indicated as arrows. (B) HEK293T cells (5×10^5) were transfected with an expression vector for wild-type or mutant TTP (0.4 μg) and then infected for 48 h with VSV-G-pseudotyped NL-Luc virus (1 ng of p24) (B) or NL-enCAT virus (1 ng of p24) (C), after which the amounts of luciferase activity (B) or CAT antigen (C) in cell lysates were determined. Data are means ± S.D. of values from three independent experiments. (D) HEK293T cells were cotransfected with pNL-enCAT (0.04 μg) and an expression vector for wild-type or mutant TTP (0.4 μg), and the amount of cellular CAT antigen was determined after incubation for 48 h. Data are means ± S.D. of values from three independent experiments. *$P < 0.05$. **$P < 0.02$.

expression of the protein, because the expression plasmid of this mutant has the same promoter as those of other mutants.

3.3. TTP influences the production of un-, single- and multiple-spliced transcripts

To examine which steps of HIV-1 replication were influenced by TTP, we next used HIV-1 reporter viruses and distinguished viral products associated with un-, single- and multiply spliced transcripts (Fig. 3A). HEK293T cells were transfected with an expression vector for wild-type or mutant TTP and then infected with the pseudotyped NL-Luc virus. The luciferase activity of the cells was increased significantly (4-fold) by wild-type TTP and to a lesser extent (1.5-fold) by the 1–101 mutant, whereas the NH_2-terminal deletion mutants 76–189 and 176–320 did not affect the luciferase activity (Fig. 3B). We then examined the expression of CAT in cells either inoculated with the NL-enCAT pseudovirus containing the HIV-1 chimeric genome of pNL-enCAT (Fig. 3A,C) or transfected with pNL-enCAT (Fig. 3A,D), both of which contain the CAT reporter gene in place of the env open reading frame [15]. In both instances, the expression of CAT was markedly inhibited by wild-type TTP or the 1–101 mutant but not by the NH_2-terminal deletion mutants 76–189 or 176–320. These results indicated that TTP promoted multiple splicing of HIV-1 transcripts, thereby increasing the products of the 2-kb spliced RNA and decreasing that of unspliced (9 kb) and single-spliced (4 kb) RNAs. Although the 1–101 mutant decreased the expression of CAT, the mutant did not significantly affect on the luciferase activity, suggesting that the mechanism of suppression of CAT activity by wild-type and the 1–101 mutant TTP seemed to be different.

To confirm that TTP affects HIV-1 replication through regulation of splicing, we co-expressed TTP and the HIV-1 clone pNL43 in HEK293T cells and examined expression levels of

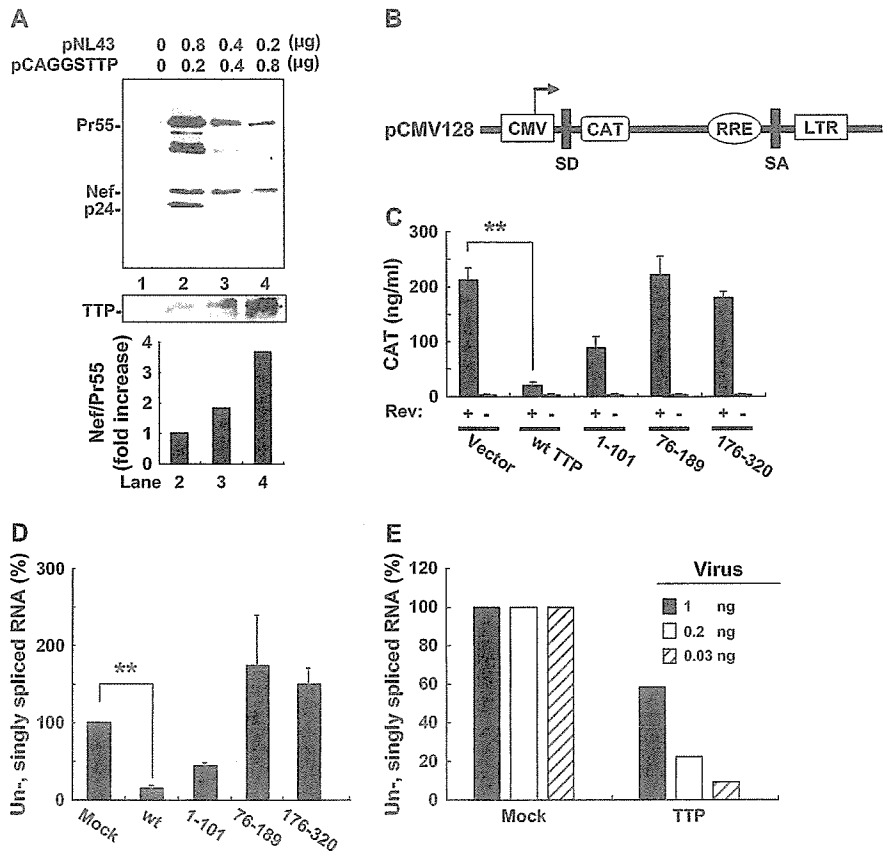

Fig. 4. Effects of TTP on HIV-1 RNA splicing. (A) HEK293T cells were cotransfected with the indicated amounts of pNL43 and of a TTP expression vector (pCAGGSTTP), after which cell lysates were subjected to immunoblot analysis with antibodies to p24 and to Nef (upper panel) or with those to TTP (lower panel). The Nef/$Pr55^{gag}$ signal ratio for the blot was determined and expressed as fold increase relative to the value for lane 2. (B) Schematic representation of the Rev reporter plasmid pCMV128. The CMV promoter (CMV), splice donor (SD), splicing acceptor (SA), and HIV-1 long terminal repeat (LTR) are indicated. (C) HEK293T cells were cotransfected with pCMV128 (0.1 μg) and an expression vector for wild-type or mutant TTP (0.4 μg) in the absence or presence of pcMax-Rev (0.4 μg). The cells were then incubated for 48 h in fresh medium before determination of the amount of intracellular CAT antigen. Data are means ± S.D. of values from three independent experiments. $^{**}P < 0.02$. (D) HEK293T cells were transfected as in (Fig. 3B) and the relative ratio of the number of un-, singly spliced transcripts (9 and 4 kb) to the number of those reactive with multiply-spliced transcripts (2 kb) was determined. Data are means ± S.D. of values from three independent experiments. (E) Cells transfected with pchTTPwt (0.4 μg) and then infected with VSV-G-pseudotyped NL-Luc virus (1, 0.2, or 0.03 ng of p24 antigen) were assayed for viral RNA splicing as in (A). Data are from a representative experiment. $^{**}P < 0.02$.

Gag and Nef proteins. Although the intracellular levels of Gag proteins (Pr55, p24) was substantially decreased by co-expression of TTP, those of Nef were not affected (Fig. 4A). The ratio of the amount of Nef to that of $Pr55^{gag}$ was found to be increased by TTP in a concentration-dependent manner (Fig. 4A). Furthermore, we investigated the effects of TTP with the use of different expression system, pCMV128, a Rev reporter plasmid that encodes most of the env sequence and a Rev-responsive element (RRE) downstream of the CAT gene, with splice donor and splice acceptor sites at the 5′ and 3′ ends of the construct, respectively [25] (Fig. 4B). Both wild-type TTP and the 1–101 mutant markedly suppressed CAT expression in HEK293T cells transfected with pCMV128 and a Rev expression plasmid, whereas the NH_2-terminal deletion mutants of TTP (76–189, 176–320) had no effect (Fig. 4C). These results thus indicated that TTP and its 1–101 mutant suppressed the Rev-induced gene expression.

3.4. Effects of TTP and its mutants on the splicing of HIV-1RNA

Because TTP decreased the products of the un-, single spliced transcripts of HIV-1 and increased multiple spliced transcripts, we examined the effects of TTP and its mutants on the splicing of HIV-1 RNA in cells transfected with pNL-Luc-E^-R^+ (Fig. 3A). Wild-type TTP induced significant decrease (86%) in the proportion of unspliced HIV-1 RNA (assessed from the ratio of the abundance of transcripts detected by the env probe to that of those detected by the tat, rev and nef cDNA probe) compared with the cells transfected with the corresponding mock vector (Fig. 4D). The TTP mutant 1–101 induced a smaller decrease (56%) in the proportion of unspliced HIV-1 RNA, whereas the NH_2-terminal deletion mutants (76–189 and 176–320) had no effect (Fig. 4D). Similar results were obtained with HEK293T cells inoculated with the VSV-G-pseudotyped NL-Luc virus (Fig. 4E). The proportion of unspliced HIV-1 RNA in cells infected with a low titer (0.03 ng of p24) of the pseudotyped NL-Luc virus was reduced by 10% by co-expression of TTP (Fig. 4E). These results thus suggested that TTP enhanced the multiple splicing of HIV-1 transcripts.

To examine whether TTP destabilizes HIV-1 RNA, we compared the effects of TTP on the RNA stability of wild-type HIV-1. However, TTP did not significantly affect the rate of RNA decay of both multiply spliced and un-, singly-spliced RNA for 180 min (data not shown).

3.5. TTP binds to HIV-1 AU-rich RNA

That AU residues of inhibitory sequence in of HIV-1 RNA can complement Rev activity [26] and replacement of AU residues of HIV-1 mRNA without alteration of the encoded proteins has been reported to result in marked expression of HIV-1 Gag, Pol, and Env proteins independent of the Rev/RRE/Crm1, suggesting that the AU-rich negative elements are necessary for the responsiveness of late HIV-1 transcripts to Rev [2,3]. As TTP binds to AU-rich elements [10], the P7 region, which has high ratio of AU residues (63%), was chosen in the HIV-1 sequence. Meanwhile, the RRE is known as a structural region bound to Rev and has relatively low AU sequence (48%). Therefore, as a control, we used a synthesized RNA of the RRE. To analyze the binding in an acrylamide gel we chose a stem loop region of the RRE, stem II, which is a minimal RNA element for Rev binding [27]. We synthesized both RNA of p7 and stem II of the RRE, which was found to contain small amount of longer substrates (Fig. 5B, black arrow). The binding assays revealed that TTP bound to P7 sequence (Fig. 5A) much more strongly than that of stem II of the RRE (Fig. 5B). To confirm that TTP specifically bound to the P7 sequence, we examined whether unlabeled P7 inhibited the binding of TTP. Unlabeled P7 RNA inhibited the binding of TTP to labeled P7 in a concentration-dependent manner, but stem II of the RRE did not (Fig. 5C).

3.6. Effects of TTP on the subcellular localization of Rev

To investigate the mechanism of suppression of HIV-1 replication by wild-type and 1–101 mutant TTP, Rev fused with

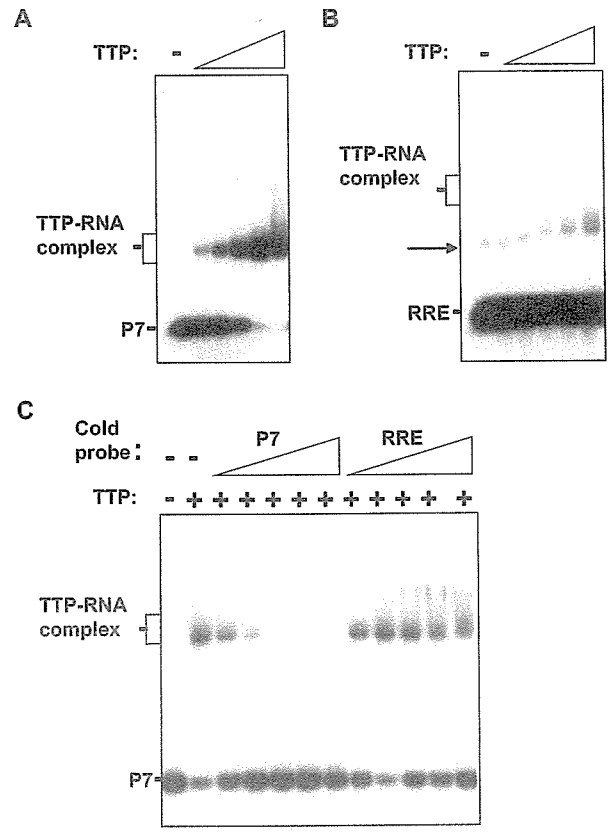

Fig. 5. Binding of TTP to the p7 RNA. Native electrophoretic mobility-shift assay of the binding of TTP (0.05, 0.1, 0.25, 0.5, or 1 μg/ml) to the ^{32}P-labeled P7 (A) or stem II of RRE (B) RNA (10 ng) in a final volume of 10 μl. Control reactions were performed in the absence of TTP(-). The positions of the free RNA molecule of P7 (75 nt), of RRE (93 nt) and of the TTP–RNA complex are indicated. (C) The binding of TTP (0.25 ng) to the ^{32}P-labeled P7 RNA (3 ng), which was mixed with different amounts of unlabeled P7 and unlabeled stem II of RRE RNA (0, 1.25, 2.5, 5, 10, and 20 ng in each lane).

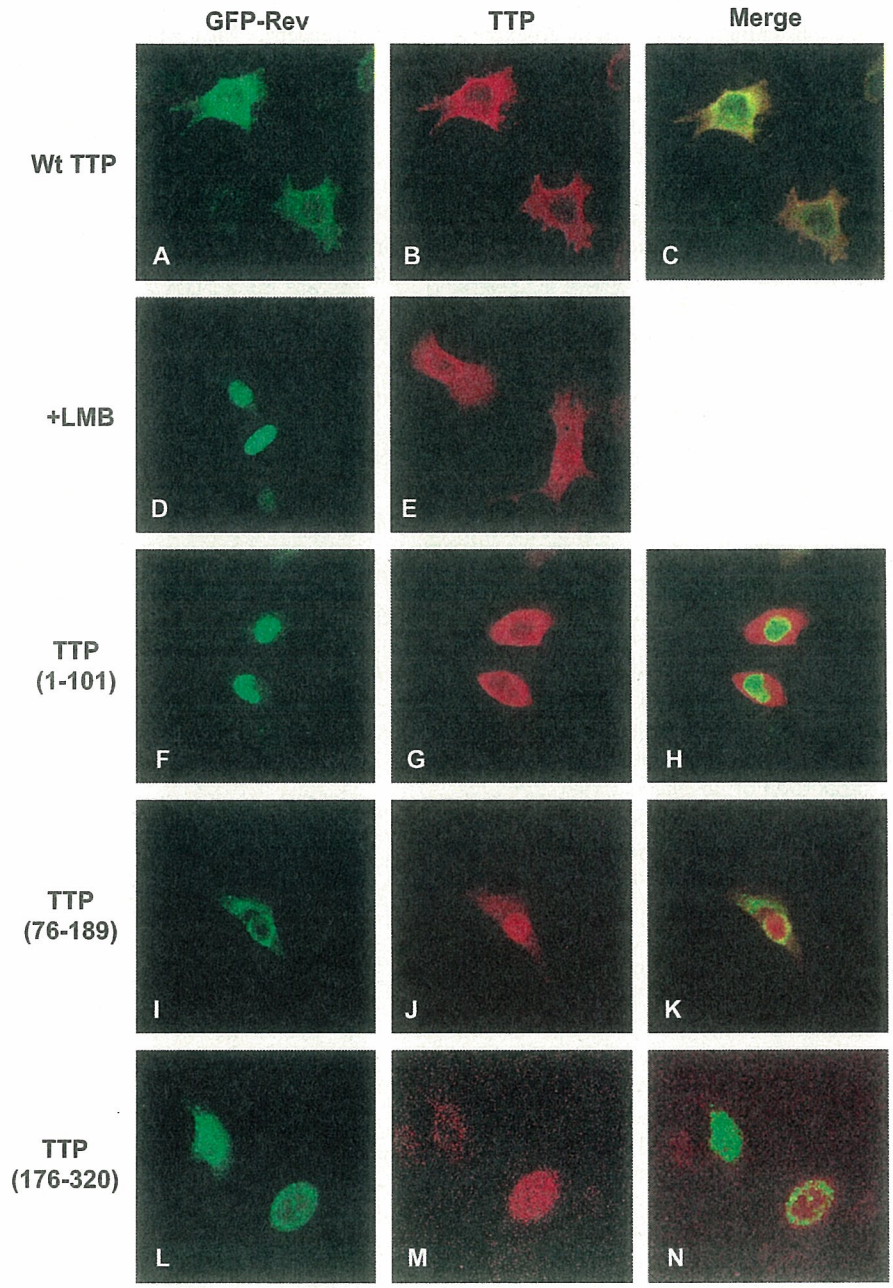

Fig. 6. Effects of TTP on the subcellular localization of Rev. HeLa cells (2.5×10^4 per well in a 12-well dish) were cotransfected with an expression plasmid for GFP-Rev (0.1 μg) and 0.3 μg of pchTTPwt (A, B, C), pcD1–101 (F, G, H), pcD76–189 (I, J, K) or pcD176–320 (L, M, N). Similarly, HeLa cells were transfected with 0.4 μg of GFP-Rev (D) or pchTTPwt (E). The cells were incubated for 90 min with leptomycin B (5 ng/ml) before analysis (D, E). The subcellular localization of GFP-Rev was monitored by GFP fluorescence (A, D, F, I, L). Immunofluorescent signals of wild-type TTP (B, E) or the mutant 1–101 (G), 76–189 (J), and 176–320 TTP (M) were examined by anti-Xpress antibody. Merged images of Rev and wild-type and mutant TTP are shown in C, H, K, and N.

marker protein, green fluorescent protein (GFP-Rev) and wild-type or the mutant TTP were co-expressed in HeLa cells (Fig. 6A–C). Both GFP-Rev and wild-type TTP were found to be localized predominantly in the cytoplasm and to a lesser extent in the nucleus and nucleolus. Singly expressed GFP-Rev or wild-type TTP showed the similar localization (data not shown). Rev and TTP are known to shuttle between the nucleolus and the cytoplasm [28]. Treatment of the cells with leptomycin B, which inhibits the CRM1-mediated nuclear export [28], resulted in the accumulation of GFP-Rev or wild-type TTP in the nucleus and nucleolus (Fig. 6D,E).

GFP-Rev was restricted to the nucleus and nucleolus in the cells expressing the TTP mutant 1–101, which itself was largely restricted to the cytoplasm (Fig. 6F–H). Both the TTP

mutant 76–189 and 176–320 did not affect on the localization of GFP-Rev (Fig. 6I–N). As has been reported previously [28], the 76–189 mutant localized in the nucleus (Fig. 6J).

4. Discussion

In the present study we have demonstrated that TTP inhibits HIV-1 production by promoting multiple splicing by direct binding to AU-rich sequences. Because TTP increased luciferase activity of NL-luc virus, which is derived from multiple spliced transcripts, inhibition of HIV-1 production was not due to nonspecific damage of the cells induced by overexpression of TTP, but due to a specific suppression by TTP binding to HIV-1 RNA.

Although the TTP mutant 1–101 lacking NLS could suppress the production derived from un-, single-spliced RNA, it did not increase the product of multiple-spliced RNA. Among the wild-type TTP and its mutants, the 1–101 mutant exclusively suppressed nuclear export of Rev similarly to leptomycin B. It is suggested that the NES sequence of the 1–101 mutant plays an important role in suppression of nuclear export of Rev. Because the 1–101 mutant is not capable of binding with RNA, marked suppression of CAT expression by the 1–101 mutant (Fig. 4C) seems to be mainly dependent on competition with Rev for binding to CRM1 which shuttles between cytoplasm and nucleus. In contrast, wild-type TTP, which directly binds to AU-rich sequence of HIV-1 RNAs, did not affect subcellular localization of Rev and increased the production of multiple-spliced RNA. Although the 76–189 mutant, which predominantly localizes in the nucleus (Fig. 6), has RNA binding activity, this mutant could not enhance the splicing HIV-1 RNA, suggesting that the nuclear localization might be related to abrogation of splicing HIV-1 RNA.

Turnover of mRNA for certain cytokines containing an ARE (AUUUA) in their 3′-untranslated region is regulated by *cis* elements and *trans*-acting factors, TTP [10]. Although sequences of HIV-1 do not contain ARE, as we found that ARE of GM-CSF mRNA was cleaved between U and A residues we expected that TTP might destabilize HIV-1 RNA, which contains AU-rich sequences [2]. However, TTP did not significantly affect HIV-1 RNA stability (data not shown). This result may be explained by the following reasons. Firstly, HIV-1 AU-rich sequences were not so effectively cleaved by TTP as ARE in GM-CSF mRNA, so we could not obtain the significant decrease of HIV-1 RNA using our assay system even in the presence of TTP. Secondly, actinomycin D in the assay system could not completely suppress the transcription of HIV-1 RNA. Other experiments would be required to demonstrate destabilization of HIV-1 RNA by TTP.

Given that TTP is exclusively expressed in activated $CD4^+$ T cells, which are targets of HIV-1, TTP might inhibit virion production in these cells and thereby inhibit the presentation of viral antigens by MHC class I molecules on the cell surface, thus contributing to persistence of an HIV-1 reservoir in T cells. The resulting inactivated cells harboring a silent HIV-1 genome might be subsequently reactivated by various stimuli and produce HIV-1 virions.

ZAP, a family of RNA binding proteins carrying CCCH-type zinc fingers, also inhibit retroviral RNA production [29]. Zinc fingers of TTP and ZAP may play an important role in nuclear retention or decay of genomic RNA with a different mechanism as RNA interference. Further studies are required to reveal the precise mechanism by which TTP affects HIV-1 RNA trafficking mediated by Rev [30].

Acknowledgments

We thank Dr. B.R. Cullen (Duke University) for providing pCMV128, pDM128/CTE and Dr. K. Ikuta (Osaka University) for the gifts of U1 cells and antibodies to Nef and p24. We also thank Dr. H. Shida (Hokkaido University) for providing pSRαRev. This work was supported in part by grants from the Ministry of Education, Science, Technology, Sports, and Culture of Japan, the Ministry of Health, Labor, and Welfare of Japan, the Japan Human Science Foundation, and the Japanese Foundation for AIDS Prevention.

References

[1] A.W. Cochrane, K.S. Jones, S. Beidas, P.J. Dillon, A.M. Skalka, C.A. Rosen, Identification and characterization of intragenic sequences which repress human immunodeficiency virus structural gene expression, J. Virol. 65 (1991) 5305–5313.

[2] W. Tan, S. Schwartz, The Rev protein of human immunodeficiency virus type 1 counteracts the effect of an AU-rich negative element in the human papillomavirus type 1 late 3′ untranslated region, J.Virol. 69 (1995) 2932–2945.

[3] M. Graf, A. Bojak, L. Deml, K. Bieler, H. Wolf, R. Wagner, Concerted action of multiple cis-acting sequences is required for Rev dependence of late human immunodeficiency virus type 1 gene expression, J.Virol. 74 (2000) 10822–10826.

[4] A.S. Zolotukhin, A. Valentin, G.N. Pavlakis, B.K. Felber, Continuous propagation of RRE(-) and Rev(-)RRE(-) human immunodeficiency virus type 1 molecular clones containing a cis-acting element of simian retrovirus type 1 in human peripheral blood lymphocytes, J. Virol. 68 (1994) 7944–7952.

[5] H. Takahashi, H. Sawa, H. Hasegawa, T. Sata, W.W. Hall, K. Nagashima, T. Kurata, Reconstitution of cleavage of human immunodeficiency virus type-1 (HIV-1) RNAs, Biochem. Biophys. Res. Commun. 293 (2002) 1084–1091.

[6] J.S. McDougal, A. Mawle, S.P. Cort, J.K. Nicholson, G.D. Cross, J.A. Scheppler-Campbell, D. Hicks, J. Sligh, Cellular tropism of the human retrovirus HTLV-III/LAV.I. Role of T cell activation and expression of the T4 antigen, J. Immunol. 135 (1985) 3151–3162.

[7] J.A. Zack, A.M. Haislip, P. Krogstad, I.S. Chen, Incompletely reverse-transcribed human immunodeficiency virus type 1 genomes in quiescent cells can function as intermediates in the retroviral life cycle, J. Virol. 66 (1992) 1717–1725.

[8] A. Clark, Post-transcriptional regulation of pro-inflammatory gene expression, Arthritis Res. 2 (2000) 172–174.

[9] A. Bevilacqua, M.C. Ceriani, S. Capaccioli, A. Nicolin, Post-transcriptional regulation of gene expression by degradation of messenger RNAs, J. Cell Physiol. 195 (2003) 356–372.

[10] N. Xu, C.Y. Chen, A.B. Shyu, Modulation of the fate of cytoplasmic mRNA by AU-rich elements: key sequence features controlling mRNA deadenylation and decay, Mol. Cell. Biol. 17 (1997) 4611–4621.

[11] T.M. Folks, J. Justement, A. Kinter, C.A. Dinarello, A.S. Fauci, Cytokine-induced expression of HIV-1 in a chronically infected promonocyte cell line. Science 238 (1987) 800–802.
[12] M. Tobiume, M. Takahoko, T. Yamada, M. Tatsumi, A. Iwamoto, M. Matsuda, Inefficient enhancement of viral infectivity and CD4 downregulation by human immunodeficiency virus type 1 Nef from Japanese long-term nonprogressors, J. Virol. 76 (2002) 5959–5965.
[13] Y. Hakata, M. Yamada, H. Shida, A multifunctional domain in human CRM1 (exportin 1) mediates RanBP3 binding and multimerization of human T-cell leukemia virus type 1 Rex protein, Mol. Cell. Biol. 23 (2003) 8751–8761.
[14] A. Adachi, H.E. Gendelman, S. Koenig, T. Folks, R. Willey, A. Rabson, M.A. Martin, Production of acquired immunodeficiency syndrome-associated retrovirus in human and nonhuman cells transfected with an infectious molecular clone, J. Virol. 59 (1986) 284–291.
[15] K. Tokunaga, A. Kojima, T. Kurata, K. Ikuta, H. Akari, A.H. Koyama, M. Kawamura, R. Inubushi, R. Shimano, A. Adachi, Enhancement of human immunodeficiency virus type 1 infectivity by Nef is producer cell-dependent, J. Gen. Virol. 79 (Pt 10) (1998) 2447–2453.
[16] R. Shibata, H. Sakai, M. Kawamura, K. Tokunaga, A. Adachi, Early replication block of human immunodeficiency virus type 1 in monkey cells, J. Gen. Virol. 76 (Pt 11) (1995) 2723–2730.
[17] T.M. Ross, B.R. Cullen, The ability of HIV type 1 to use CCR-3 as a coreceptor is controlled by envelope V1/V2 sequences acting in conjunction with a CCR-5 tropic V3 loop, Proc. Natl. Acad. Sci. USA 95 (1998) 7682–7686.
[18] R.A. Fouchier, B.E. Meyer, J.H. Simon, U. Fischer, M.H. Malim, HIV-1 infection of non-dividing cells: evidence that the amino-terminal basic region of the viral matrix protein is important for Gag processing but not for post-entry nuclear import, EMBO J 16 (1997) 4531–4539.
[19] G.A. Taylor, W.S. Lai, R.J. Oakey, M.F. Seldin, T.B. Shows, R.L. Eddy Jr., P.J. Blackshear, The human TTP protein: sequence, alignment with related proteins, and chromosomal localization of the mouse and human genes, Nucleic Acids Res. 19 (1991) 3454.
[20] Z. Tsuchihashi, P.O. Brown, DNA strand exchange and selective DNA annealing promoted by the human immunodeficiency virus type 1 nucleocapsid protein, J. Virol. 68 (1994) 5863–5870.
[21] D.P. Bednarik, T.M. Folks, Mechanisms of HIV-1 latency, AIDS 6 (1992) 3–16.
[22] M. Tobiume, K. Fujinaga, M. Kameoka, T. Kimura, T. Nakaya, T. Yamada, K. Ikuta, Dependence on host cell cycle for activation of human immunodeficiency virus type 1 gene expression from latency, J. Gen. Virol. 79 (Pt 6) (1998) 1363–1371.
[23] A.M. Fairhurst, J.E. Connolly, K.A. Hintz, N.J. Goulding, A.J. Rassias, M.P. Yeager, W. Rigby, P.K. Wallace, Regulation and localization of endogenous human tristetraprolin, Arthritis Res. Ther. 5 (2003) R214–R225.
[24] K. Tokunaga, M.L. Greenberg, M.A. Morse, R.I. Cumming, H.K. Lyerly, B.R. Cullen, Molecular basis for cell tropism of CXCR4-dependent human immunodeficiency virus type 1 isolates, J. Virol. 75 (2001) 6776–6785.
[25] Y. Luo, H. Yu, B.M. Peterlin, Cellular protein modulates effects of human immunodeficiency virus type 1 Rev, J. Virol. 68 (1994) 3850–3856.
[26] I. Mikaelian, M. Krieg, M.J. Gait, J. Karn, Interactions of INS (CRS) elements and the splicing machinery regulate the production of Rev-responsive mRNAs, J. Mol. Biol. 257 (1996) 246–264.
[27] K.S. Cook, G.J. Fisk, J. Hauber, N. Usman, T.J. Daly, J.R. Rusche, Characterization of HIV-1 REV protein: binding stoichiometry and minimal RNA substrate, Nucleic Acids Res. 19 (1991) 1577–1583.
[28] T. Murata, Y. Yoshino, N. Morita, N. Kaneda, Identification of nuclear import and export signals within the structure of the zinc finger protein TIS11, Biochem. Biophys. Res. Commun. 293 (2002) 1242–1247.
[29] G. Gao, X. Guo, S.P. Goff, Inhibition of retroviral RNA production by ZAP, a CCCH-type zinc finger protein, Science 297 (2002) 1703–1706.
[30] N. Sanchez-Velar, E.B. Udofia, Z. Yu, M.L. Zapp, hRIP, a cellular cofactor for Rev function, promotes release of HIV RNAs from the perinuclear region, Genes Dev. 18 (2004) 23–34.

AML1/Runx1 rescues Notch1-null mutation-induced deficiency of para-aortic splanchnopleural hematopoiesis

Masahiro Nakagawa, Motoshi Ichikawa, Keiki Kumano, Susumu Goyama, Masahito Kawazu, Takashi Asai, Seishi Ogawa, Mineo Kurokawa, and Shigeru Chiba

The Notch1-RBP-Jκ and the transcription factor Runx1 pathways have been independently shown to be indispensable for the establishment of definitive hematopoiesis. Importantly, expression of Runx1 is down-regulated in the para-aortic splanchnopleural (P-Sp) region of *Notch1*- and *Rbpsuh*-null mice. Here we demonstrate that Notch1 up-regulates Runx1 expression and that the defective hematopoietic potential of *Notch1*-null P-Sp cells is successfully rescued in the OP9 culture system by retroviral transfer of Runx1. We also show that Hes1, a known effector of Notch signaling, potentiates Runx1-mediated transactivation. Together with the recent findings in zebrafish, Runx1 is postulated to be a cardinal downstream mediator of Notch signaling in hematopoietic development throughout vertebrates. Our findings also suggest that Notch signaling may modulate both expression and transcriptional activity of Runx1. (Blood. 2006;108:3329-3334)

Introduction

Mammalian hematopoietic development is believed to arise from 2 distinct cellular origins. In mice, primitive hematopoiesis arises in the yolk sac (YS) blood island at embryonic day (E) 7.5, while definitive hematopoiesis starts at the ventral region of the aorta-gonad-mesonephros (AGM) around E10.5, which shifts to the liver, spleen, and bone marrow, in this order. Progenitors for definitive hematopoiesis are first detected in the para-aortic splanchnopleural (P-Sp) region at E7.5 to E9.5,[1,2] where the *Notch1* gene has a nonredundant role in hematopoietic stem cell (HSC) development.[3] *Notch1* encodes a 300-kDa heterodimeric single-span transmembrane receptor consisting of a 180-kDa extracellular and a 120-kDa transmembrane subunit. Together with 3 other paralogs, it belongs to the evolutionarily conserved Notch family receptors that mediate cell-fate determination in multiple species. The Notch signaling is initiated by the binding of the Jagged and Delta families of ligands expressed on the neighboring cells, which induces the cleavage of the Notch transmembrane subunit and the release of the Notch intracellular domain. The latter in turn translocates to the nucleus and forms a transactivation complex by interacting with the DNA-binding protein RBP-Jκ and induces the expression of their target genes, such as those for the hairy/enhancer of split (*Hes*) family of basic helix-loop-helix transcription factors.[4] Molecular channels downstream of these, however, are largely unknown.

Mice deficient in *Runx1* (also known as *AML1*, *CBFA2*, or *PEBP2αB*), *Scl*, and *Gata2* genes are lethal during the embryonic stage and show failure in the establishment of definitive hematopoiesis.[5-7] A connection between Notch signaling and these transcription factors has been shown by the analyses of *Notch1*- and RBP-Jκ–encoding *Rbpsuh*-null mice. In the E9.5 P-Sp cells from *Notch1*-null mice, expression levels of SCL, GATA2, and Runx1 mRNA are significantly reduced.[3] *Rbpsuh*-null mice also show markedly reduced levels of SCL, GATA2, and Runx1 mRNA in the endothelial-cell layer of the E9.5 P-Sp region,[8] supporting the notion that the Notch1-RBP-Jκ pathway up-regulates the expression of these key transcription factors. Among these, Runx1, which has close homology to a *Drosophila* protein, Runt, functions as a transcriptional activator or repressor for its target genes in concert with several specific coactivators or corepressors, depending on the context.[9] Importantly, presence of the Notch-Runx pathway has been proposed in *Drosophila* embryonic hemocytogenesis[10] and zebrafish hematopoiesis during both developmental and postnatal periods.[11] Similarly reported has been transcriptional regulation by Notch of the *Gata2* gene in mouse AGM hematopoiesis[8] and of the *Gata* homolog *Serpent* gene in *Drosophila* embryonic hemocytogenesis.[12] In mammals, the existence of Notch-Runx pathway has been unclear.

In this study, we show that Notch1 up-regulates Runx1 mRNA expression in NIH3T3 cells. When introduced to the defective prehematopoietic precursor cells derived from the P-Sp region of *Notch1*-null embryos using retroviruses, Runx1, but neither SCL nor GATA2, restores the definitive hematopoiesis. We also demonstrate that Hes1, one of the Notch signal effectors, augments the transcriptional activity of Runx1 protein. These findings indicate that Runx1 is a key molecule in Notch1-RBP-Jκ–mediated mammalian hematopoiesis.

From the Departments of Hematology and Oncology and Regeneration Medicine for Hematopoiesis, Graduate School of Medicine, University of Tokyo, Japan; and the Department of Cell Therapy and Transplantation Medicine, University of Tokyo Hospital, Tokyo, Japan.

Submitted April 25, 2006; accepted July 3, 2006. Prepublished online as *Blood* First Edition Paper, August 3, 2006; DOI 10.1182/blood-2006-04-019570.

Supported in part by Grant-in-Aid for Scientific Research (KAKENHI no. 17390274) and Grant-in-Aid for Japan Society for the Promotion of Science (JSPS), Fellows from JSPS, Research on Pharmaceutical and Medical Safety, Health and Labour Sciences Research Grants, Ministry of Health, Labour and Welfare of Japan.

The authors declare no competing financial interests.

Reprints: Shigeru Chiba, Department of Cell Therapy and Transplantation Medicine, University of Tokyo Hospital, 7-3-1 Hongo, Bunkyo-ku, Tokyo 113-8655, Japan; e-mail: schiba-tky@umin.ac.jp.

The publication costs of this article were defrayed in part by page charge payment. Therefore, and solely to indicate this fact, this article is hereby marked "advertisement" in accordance with 18 USC section 1734.

Materials and methods

Mice and embryos

C57BL/6 mice were purchased from Japan SLC (Hamamatsu, Japan) and *Notch1* mutant mice[13] were from Jackson Laboratory (Bar Harbor, ME). To generate embryos, timed matings were set up between *Notch1*$^{+/-}$ mice. The time at midday (12 PM) was taken to be E0.5 for the plugged mice.

In vitro P-Sp culture

P-Sp culture was performed as described previously.[14] In brief, isolated P-Sp regions of E9.5 embryos were dissociated by incubation with 250 protease units (PU)/mL dispase (Godo Shusei, Tokyo, Japan) for 20 minutes and cell-dissociation buffer (Gibco BRL, Carlsbad, CA) for 20 minutes at 37°C, followed by vigorous pipetting. Approximately 5×10^4 P-Sp–derived cells were suspended in 300 μL of serum-free StemPro media (Life Technologies, Gaithersburg, MD) supplemented with 50 ng/mL stem-cell factor (SCF), 5 ng/mL interleukin-3 (IL3; gifts from Kirin Brewery, Takasaki, Japan), and 10 ng/mL mouse oncostatin M (R&D Systems, Minneapolis, MN). Single-cell suspensions were seeded on preplated OP9 stromal cells[15] in the 24-well plate, followed by incubation at 37°C in a 5% CO_2 incubator. Images were visualized with a Nikon Eclipse TE2000-U microscope equipped with 40×/0.60 and 10×/0.30 NA objective lenses (Nikon, Tokyo, Japan), and were captured with a C5810 camera (Hamamatsu Photonics, Hamamatsu, Japan).

Plasmid construction

The cDNA of human Runx1 was subcloned into the *Eco*RI restriction site of the retrovirus vector pMYs/internal ribosomal entry site–enhanced green fluorescent protein (IRESEGFP; pMYs/IG).[16] The cDNAs for FLAG-tagged murine SCL and FLAG-tagged murine GATA2 were inserted into the *Eco*RI and *Not*I restriction sites of pMYs/IG. The cDNA for murine Notch1 intracellular domain (NICD)[3] was subcloned into the *Bam*HI restriction site of pMYs/IG. To assess the domain functions of Runx1, we used mutants and wild-type Runx1 constructed in pMY/IG.[14] The pME18S-HA-Runx1 and pME18S-PEBP2β were described previously.[17] The cDNA for FLAG-tagged murine Hes1 was inserted into the *Eco*RI and *Not*I restriction sites of the pME18S-expression vector and in-frame into the *Eco*RI and *Xba*I restriction sites of the p3xFLAG-myc-CMV-25–expression vector (Sigma, St Louis, MO).

Retroviral transduction

Plat-E packaging cells (2×10^6)[16] were transiently transfected with 3 μg of retrovirus vectors, mixed with 9 μL of FuGENE6 (Roche Applied Science, Indianapolis, IN), and incubated at 37°C. Supernatant containing retrovirus was collected 48 hours after transfection and used immediately for infection. Retroviral transduction of the cells derived from *Notch1*-null P-Sp regions was performed as described previously.[14] In brief, the viral supernatant was added to the P-Sp cells seeded on the OP9 stromal-cell layer together with 10 μg/mL polybrene (Sigma). After 72 hours of incubation, virus-containing medium was replaced by the original culture medium. The cells were incubated for another 10 days and processed for analysis. To confirm the expression of proteins, NIH3T3 cells were also infected with the same viral supernatants. The efficiency of infection was evaluated by the positivity of GFP. The proteins were detected by Western blot using anti-Runx1 antibody (PC284L; Oncogene, Cambridge, MA), anti-FLAG monoclonal antibody (M2; Sigma), and anti-FLAG polyclonal antibody (F7425; Sigma) to detect Runx1, GATA2, and SCL, respectively. F7425 antibody was used to exclude the overlap of SCL and nonspecific band by M2 antibody.

CFC assay

The nonadherent or semiadherent cells that emerged from wild-type and *Notch1*-null P-Sp regions were used for colony-forming–cell (CFC) assays. Cells (6×10^4) were plated into MethoCult GF M3434 medium (StemCell Technologies, Vancouver, BC, Canada) and cultured in a 5% CO_2 incubator at 37°C. Colony types were determined at day 7 by morphologic appearance and by Wright-Giemsa staining of each colony. Images were taken with a Nikon Eclipse TE2000-U.

Flow cytometric analysis

Flow cytometric analysis was performed with a BD LSRII (BD Biosciences, San Jose, CA) after addition of 7-amino-actinomycin D (7-AAD) (Via-Probe; BD PharMingen, San Diego, CA) to exclude dead cells. For surface staining, cell suspensions collected from the P-Sp cultures were incubated on ice for 30 minutes in the presence of various mixtures of labeled monoclonal antibodies. The following monoclonal antibodies were purchased from BD PharMingen: phycoerythrin (PE)–conjugated anti–granulocyte 1 (anti–Gr-1), anti–macrophage antigen 1 (anti–Mac-1), anti–stem-cell antigen 1 (anti–Sca-1), anti–Ter-119, allophycocyanin (APC)–conjugated anti-CD45, anti–c-Kit, and biotin-conjugated anti-CD34. Biotinylated antibodies were labeled with PE- or APC-conjugated streptavidin.

Immunoprecipitation and Western blotting

COS7 cells were transfected with expression plasmids (pME-HA-Runx1 and p3xFLAG-myc-CMV-25-Hes1) using the FuGENE6 according to the manufacturer's instruction. The cells were cultured in Dulbecco modified Eagle medium (DMEM) supplemented with 10% fetal calf serum (FCS) for 48 hours after transfection and were lysed in radioimmunoprecipitation assay (RIPA) buffer.[14] These cell lysates were precleared with protein G–sepharose (Amersham Bioscience, Little Chalfont, United Kingdom) and mixed with anti-FLAG antibody (M2; Sigma) or anti-HA antibody (HA.11; Covance Research Products, Berkeley, CA) for 2 hours. The antibody-associated proteins were then recovered on protein G–sepharose beads. The beads were washed 4 times with the RIPA buffer. Whole-cell lysates containing 100 μg of proteins and immunoprecipitates were subjected to 10% sodium dodecyl sulfate–polyacrylamide gel electrophoresis (SDS-PAGE) and transferred to polyvinylidene difluoride membranes (Immobilon; Millipore, Bedford, MA). The membranes were blocked with 5% skim milk treated with either peroxidase-conjugated anti-FLAG monoclonal antibody (M2; Sigma) or peroxidase-conjugated anti-HA monoclonal antibody (12CA5; Roche Applied Science). The blots were visualized using the enhanced chemiluminescence (ECL) system (Amersham Bioscience).

Transcriptional response assays

Luciferase assays were performed as described previously[18] with minor modifications. Briefly, HeLa cells were transfected with 300 ng of reporter (pM-CSF-R-luc),[19] and expression plasmids (combinations of 200 ng of pME18S-HA-Runx1 and 160 ng of pME18S-PEBP2β and 60, 200, or 600 ng of pME18S-FLAG-Hes1 or control) using FuGENE6 according to the manufacturer's instructions. As a control of transfection efficiency, a plasmid expressing β-galactosidase was cotransfected. The cells were harvested 48 hours after transfection and assayed for luciferase activity. The data were normalized to β-galactosidase activity.

Quantitative PCR analysis

NIH3T3 cells were infected with NICD or mock retrovirus. The cells were cultured in DMEM medium supplemented with 10% FCS for 48 hours after infection and were selected by the expression of GFP with the FACSAria (BD Biosciences). Total cellular RNA was extracted with RNeasy (QIAGEN, Hilden, Germany) and converted into cDNAs by reverse transcriptase (Superscript III; Invitrogen, Carisbad, CA). Real-time polymerase chain reaction (PCR) was performed using TaqMan Gene Expression Assays Mm00486762_m1 (Applied Biosystems, Foster City, CA) with the ABI PRISM 7000 Sequence Detection System (Applied Biosystems) according to the manufacturer's instructions. Amplification of 18S ribosomal RNA cDNA was used as the endogenous normalization standard.

Results

Retroviral expression of Runx1 rescues hematopoietic defects of *Notch1*-null P-Sp regions

It has been reported that expression of Runx1 or its homolog, *Lozenge*, is up-regulated by positive Notch signaling in zebrafish and *Drosophila* systems, respectively.[10,11] We thus first evaluated whether Notch activation results in up-regulation of Runx1 also in the mammalian system. When NIH3T3 cells were transiently transfected with Notch1 intracellular domain (NICD), which represents the constitutive active form of Notch1, the mRNA level of Runx1 increased (Table 1).

We then examined whether forced expression of Runx1 could rescue the hematopoietic defect of *Notch1*-null mice. Wild-type P-Sp cells gave rise to round-shaped nonadherent cells when overlayed on the OP9 stromal cells. Flow cytometric analysis of these cells revealed that they were viable (7-AAD negative) CD45-positive cells (top panels in Figure 1A), representing hematopoietic cells. No such cells were generated from *Notch1*-null P-Sp cells and only background OP9 cells were observed (bottom panels in Figure 1A).[3] We retrovirally infected *Notch1*-null P-Sp cells that were seeded on the OP9 layer with Runx1, SCL, or GATA2, and assessed whether *Notch1*-null P-Sp cells could generate hematopoietic cells. Titers of the retroviruses containing Runx1, SCL, and GATA2 were similar to each other as evaluated by infecting NIH3T3 cells with these viruses (Figure 2A). Expression of individual proteins was confirmed by a Western blot analysis (Figure 2B). Mock, SCL, and GATA2 transduction did not generate round-shaped nonadherent cells morphologically or viable CD45-positive cells detectable by flow cytometric analysis. In contrast, Runx1-transduced P-Sp cells gave rise to round-shaped nonadherent cells. These cells were shown to be viable CD45-positive cells by flow cytometric analysis (Figure 1B). This pattern was identical to the positive control (Notch1$^{+/+}$ P-Sp cells; top panels in Figure 1A).

To confirm that the cells developed from Runx1-infected *Notch1*-null P-Sp cells (hereafter referred to as Runx1-rescued cells) retain the features of hematopoietic cells, we evaluated these cells for surface markers and CFC activities. The flow cytometric analysis of the Runx1-rescued cells at day 12 revealed that they express hematopoietic cell-surface markers such as a panleukocyte marker (CD45), stem-cell markers (c-Kit, CD34, and Sca1), myeloid-cell markers (Gr-1 or Mac-1), and an erythroid-cell marker (Ter-119) (Figure 3A). Their expression profiles were reminiscent of those of hematopoietic cells generated from the wild-type P-Sp cells (Figure 3B). The P-Sp culture system faithfully reproduced the generation of hematopoietic cells, and there were no consistent differences between Runx1-rescued and wild-type P-Sp–derived cells in the surface-marker expression levels, although we observed variable minor differences in individual experiments partly because of the variation in the time required for hematopoietic development (Figure 3A-B).

When the Runx1-rescued cells were seeded into semisolid medium at day 12 and cultured for an additional 7 days, they generated mixed, granulocyte/macrophage, and erythroid colonies containing enucleated erythrocytes (Figure 4A) at a frequency comparable to that of wild-type P-Sp–derived cells (Figure 4B-C). There were no statistical differences in the numbers of total ($P = .11$) and individual (erythroid, $P = .20$; granulocyte/macrophage, $P = .11$; mixed, $P = .07$) colonies generated from *Notch1*$^{+/+}$

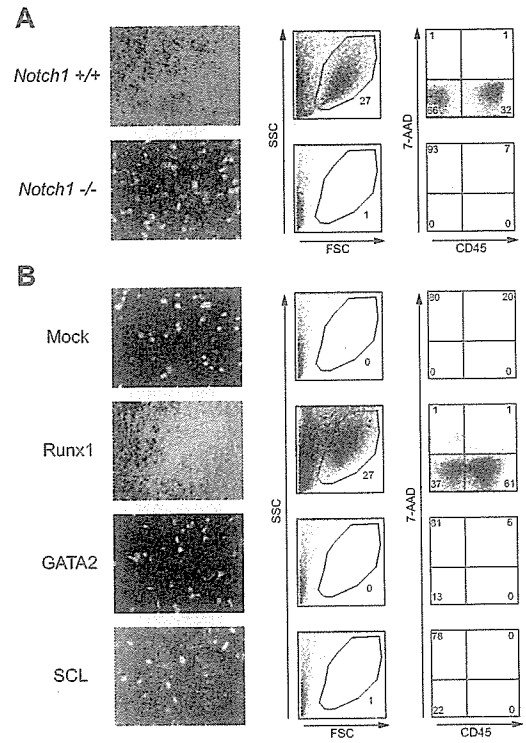

Figure 1. Retroviral expression of Runx1 rescues hematopoietic defect of *Notch1*-null P-Sp region. (A) P-Sp cells from wild-type (*Notch1*$^{+/+}$) and *Notch1*-null (*Notch1*$^{-/-}$) embryos at E9.5 were cultured for 5 days on OP9 cells. (B) P-Sp cells from *Notch1*-null embryos at E9.5 were infected with mock retrovirus or retrovirus containing Runx1, SCL, or GATA2, and cultured for 12 days on OP9 cells. Microscopic representation (left column; original magnification, × 100). Only cocultured OP9 cells are shown if hematopoietic cells are not produced. Flow cytometric analyses (center and right columns) of cells generated in the culture. Percentages of cells gated (center columns) and cells in each quadrant (right columns) are indicated.

Table 1. Notch activation up-regulates the expression of Runx1

	RAU	Mean	Notch-mock
Experiment 1			2.78*
NIH3T3-Mock	0.112634; 0.077514; 0.093663	0.094604	
NIH3T3-Notch	0.263982; 0.241864; 0.282636	0.262827	
Experiment 2			4.12*
NIH3T3-Mock	0.038500; 0.045755; 0.044123	0.042792	
NIH3T3-Notch	0.186016; 0.148638; 0.194443	0.176366	

Data are from 2 independent experiments in triplicate. RAU, relative arbitrary units; Notch-mock, the ratio of RAU by constitutive active Notch 1 infection and RAU by mock infection.

*$P < .01$ (2-tailed, unequal variance t test).

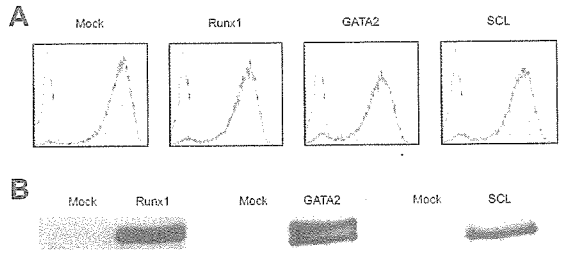

Figure 2. Retroviruses properly create Runx1, GATA2, and SCL proteins. (A) The efficiency of retrovirus-mediated gene transfer of Runx1, GATA2, or SCL was estimated by infecting NIH3T3 cells. Retrovirus-infected cells were evaluated by the expression of GFP (shaded histograms). Uninfected NIH3T3 cells are also shown as a control (open histograms). (B) Expression of individual proteins was confirmed by a Western blot analysis.

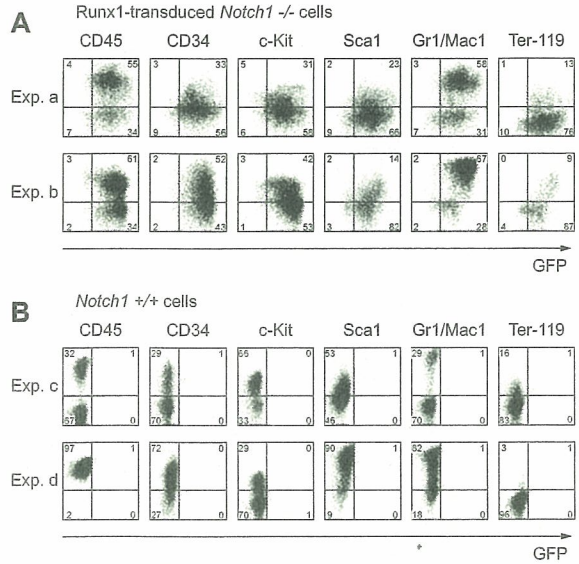

Figure 3. Runx1-rescued cells express hematopoietic surface markers. Expression of hematopoietic surface markers of cultured cells at day 12 from Runx1-transduced *Notch1*-null (*Notch1*$^{-/-}$) embryos (A) or wild-type (*Notch1*$^{+/+}$) embryos (B) was evaluated by flow cytometric analyses. GFP intensity (marking retrovirus-transduced cells) is plotted on the x-axis and intensity of counterstaining of hematopoietic surface markers is plotted on the y-axis. The results show representative results of independent replicates from 5 experiments. Percentages of cells in each quadrant are indicated.

and Runx1-transduced *Notch1*$^{-/-}$ P-Sp–derived cells. These observations indicate that the hematopoietic characteristics of Runx1-rescued cells were similar to those of wild-type P-Sp–derived cells.

Functional implication of Runx1 at the downstream of Notch-RBP-Jκ pathway

Runx1 has several distinct domains with defined biochemical functions. The Runt domain mediates both binding to DNA and dimerization with a partner protein, CBFβ/PEBP2β, whereas the transactivation domain interacts with transcriptional coactivators. Inhibitory domain counteracts the effect of the transactivation domain. The VWRPY motif located near the C-terminus mediates the interaction with a corepressor, TLE. A domain that interacts with mSin3A corepressor is also identified.[9] To assess whether Runx1 functions as an activator or a repressor[20] to restore the hematopoietic defect of *Notch1*-null embryo, we examined a series of Runx1 mutants (Figure 5)[14] for hematopoietic rescue.

Infection of retroviruses containing wild-type and several mutants, Δ444, Δ397, and Δ205-332 of Runx1 (Figure 5) resulted in the rescue of the *Notch1*-null phenotype, giving the same pattern with the culture of wild-type P-Sp cells (Figure 1A, top panels). In contrast, other mutants, Δ335, Δ288, AML1a, ΔRD, Δ205-332, and R139G (Figure 5) could not rescue the *Notch1*-null phenotype, giving the same pattern with the negative control (Figure 1A, bottom panels). Therefore, wild-type of Runx1 and the mutants that lack the VWRPY domain (Δ444, Δ397) or the mSin3A-binding region (Δ181-210) could restore the production of hematopoietic cells in the *Notch1*-null P-Sp culture, whereas those mutants that lack transactivation domain (Δ335, Δ288, AML1a, and Δ205-332) or Runt domain (ΔRD) could not rescue hematopoiesis from the *Notch1*-null P-Sp cells. Since changes in the tertiary structure of the protein could influence the function independent of the role of each domain, we also examined R139G, a mutant isolated from a patient with myelodysplastic syndrome (MDS) that harbors a point mutation causing substitution of Arg139 in the Runt domain with Gly. The DNA-binding ability is severely impaired in R139G, although the ability to heterodimerize with CBFβ/PEBP2β is spared.[21] This mutant could not restore hematopoiesis. These results suggest that, in the presence of an intact Runt domain, the transcriptional activating function is necessary and sufficient for Runx1 to rescue the hematopoietic defect of *Notch1*-null mice in the P-Sp culture system, while the transcriptional repressing function is dispensable.

Notch signaling also regulates transactivating function of Runx1

Hes1 is known to be a canonical Notch-RBP-Jκ target gene in mammals. It is also evident, however, by a number of studies that Hes1 mediates a part of, but not the whole, Notch-RBP-Jκ signaling.[22] In adult hematopoiesis, Hes1 maintains HSCs in vitro and expands them in vivo when retrovirally introduced to a highly HSC-enriched population.[23] Because Hes1 is expressed in the hematopoietic clusters budding from the dorsal aorta,[8] this transcription factor is a candidate as a physiologic target of the Notch-RBP-Jκ pathway in the embryonic hematopoietic development. Hes1 has also been known to mediate cross-talk between Notch and

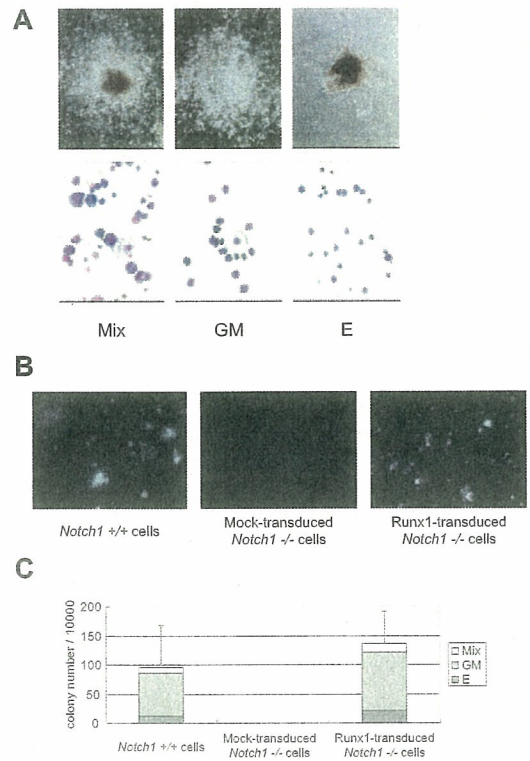

Figure 4. Runx1-rescued cells generate hematopoietic colonies. Colony formation of the Runx1-rescued cells from *Notch1*-null embryos. The rescued cells were harvested at day 12 and plated into MethoCult GF M3434 medium. (A) Representative hematopoietic colonies at day 7 are shown. Mix indicates mixed colony; GM, granulocyte/macrophage colony; and E, erythroid colony. Morphology of the colonies (top panels); original magnification, × 100. Wright-Giemsa–stained cytospin preparation of corresponding cell populations (bottom panels); original magnification, × 600. (B) Photographs of representative colonies. Original magnification, × 3. (C) The total number of colonies and the frequencies of different kinds of colonies. The results show the mean values of 5 independent experiments, each in duplicate, with standard deviations for the total colony numbers. Data were statistically analyzed by 2-tailed, unequal-variance *t* test.

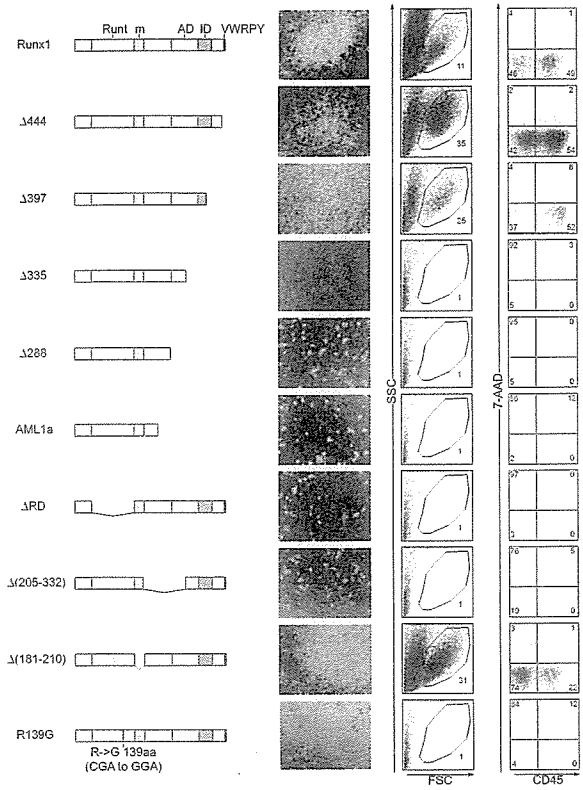

Figure 5. The transcriptionally active form of Runx1 is required for hematopoietic rescue. P-Sp cells from *Notch1*-null embryos at E 9.5 were infected with retroviruses containing *Runx1* mutants and cultured on OP9 cells for 12 days. Structures of Runx1 mutants are depicted (left column). Runt indicates the Runt domain; m, a binding region for mSin3A; AD, transactivation domain; ID, inhibitory domain; and VWRPY, VWRPY motif. Microscopic representations (center column; original magnification, × 100) and flow cytometric analyses (right 2 columns) of cells produced in the culture. Percentages of cells gated (center columns) and cells in each quadrant (right columns) are indicated.

other signaling pathways such as Janus-activating kinase/signal transducer and activator of transcription (JAK/STAT), Wnt, and Ras/mitogen-activated protein kinase (MAPK) pathways.[24-26] Furthermore, the transactivating function of Runx2, another Runx family member, is modified by Hes proteins and their relatives Hey proteins. When overexpressed, Hes1 potentiates Runx2-mediated transactivation in the transfected cells,[27] while Hey represses Runx2-mediated transactivation.[28,29]

Based on these pieces of information, we assessed whether Hes1 also modulates Runx1-mediated transactivation. Consistent with a previous report in which Hes1 was shown to bind to Runx1 in glutathione S-tranferase (GST) pull-down assays,[27] we detected HA-tagged Runx1 protein in the anti-FLAG immunoprecipitant, and reversely, FLAG-tagged Hes1 protein in the anti-HA immunoprecipitant, indicating physical interaction of Hes1 with Runx1 (Figure 6A). Moreover, Hes1 potentiated Runx1-mediated transactivation when expressed in HeLa cells, depending on the expression levels of Hes1 (Figure 6B).

Discussion

In this study, we showed that Runx1 rescues the defective hematopoiesis of *Notch1*-null mice in the OP9 culture system. The functional relationship between Notch and Runx families during hematopoietic development was first indicated in *Drosophila*, in which Notch up-regulates the expression of a *Runt* family gene, *Lozenge*.[10] More recently, it was shown that a zebrafish Notch-signaling mutant *mind bomb* fails in the specification of definitive HSCs during embryogenesis, and that Runx1 is required for expansion of HSCs in the zebrafish AGM region sufficient to restore the HSC specification in the *mind bomb* mutant.[11] The data shown in the present study strongly indicate that the Notch-Runx pathway is conserved from invertebrates to mammals and that Runx1 locates at a very proximal position in the Notch1 signaling pathway during establishment of definitive hematopoiesis.

GATA2 is also reported to have an important role downstream of Notch signaling in the establishment of definitive hematopoiesis. It was reported that NICD directly binds to the *Gata2* promoter and increases its expression level in mouse AGM cells.[8] Similarly in *Drosophila*, Notch up-regulates *Serpent* and induces emergence of hemocyte progenitors in lymph glands.[12] In our retroviral expression system, however, GATA2 could not rescue the hematopoietic defect of *Notch1*-null P-Sp cells (Figure 1B). It remains unknown whether GATA2 expression in more regulated levels and/or timings could rescue the hematopoietic deficient phenotype of *Notch1*-knockout P-Sp cells.

We clearly demonstrated that definitive hematopoiesis is rescued by forced expression of Runx1 in the *Notch1*-null P-Sp cells, but it should be directly shown whether transplantable HSCs are generated from the *Notch1*-null Runx1-introduced P-Sp cells. Fresh P-Sp cells obtained from wild-type embryos can be engrafted

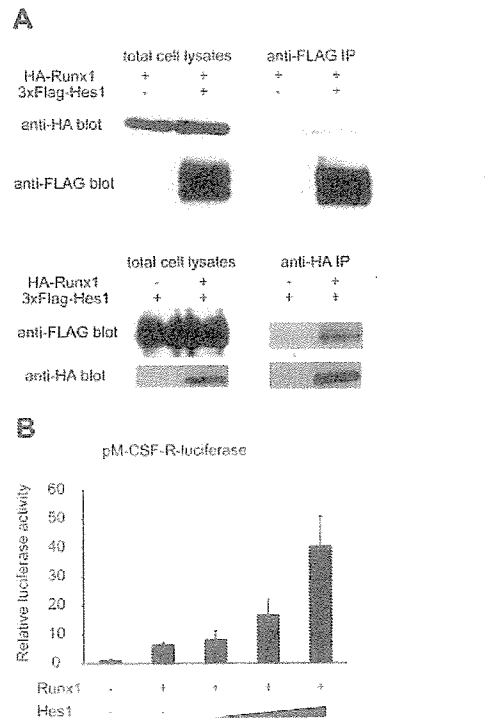

Figure 6. Notch signaling regulates transcriptional level of Runx1 and modulates the function of Runx1 protein through the effector protein, Hes1. (A) COS7 cells were transfected with HA-tagged Runx1 and 3xFLAG-tagged Hes1. Whole-cell extracts were immunoprecipitated (IP) with anti-FLAG antibody or anti-HA antibody followed by immunoblotting (blot) using anti-HA antibody or anti-FLAG antibody. (B) Relative luciferase activity in HeLa cells transfected with Runx1 (200 ng) and Runx1-dependent macrophage colony-stimulating factor receptor (pM-CSF-R) luciferase reporter (300 ng) with or without cotransfection of Hes1 (60, 200, or 600 ng). Data are means ± standard errors of duplicate wells in a representative experiment. Reproducible results were obtained in 3 independent experiments.

to mouse bone marrow if injected in the preconditioned newborn mice, as described.[3,30] It is unknown, however, whether the cultured P-Sp cells are also engraftable with the same method. We were unable to observe engraftment of the cultured P-Sp cells unlike fresh P-Sp cells, when injected to busulfan-pretreated newborn mice (data not shown). Culturing the cells, even for just a short time, is prerequisite for the retroviral gene transfer, which stands as a major technical obstacle to assess the engraftability of the *Notch1*-null Runx1-introduced P-Sp cells. Transgenic expression of Runx1, under an appropriate promoter, in the *Notch1*-null background may reveal further that the Notch1-Runx1 pathway represents an essential physiologic channel for the mammalian HSC generation from the P-Sp cells.

We also showed that Hes1, a known mediator of Notch signaling, cooperatively activates the Runx1-responsive pM-CSF-R luciferase reporter. This observation suggests that the Notch1 pathway modulates expression of Runx1 target genes through multiple mechanisms. There is a possibility that Notch1 directly augments the expression of Runx1 target genes. Although overexpression of Runx1 is sufficient to restore hematopoietic potential in *Notch1*-null P-Sp cells, both of these mechanisms might cooperatively contribute to HSC generation during normal development.

Acknowledgments

We thank M. Ohki for the gift of the human Runx1 cDNA, Y. Ito for the PEBP2β cDNA, D.-E. Zhang for the pM-CSF-R-luc vector, T. Kitamura for the Plat-E packaging cells and the pMYs/IRES-EGFP retrovirus vector, T. Nakano for the OP9 stromal cells, R. Kageyama for the Hes1 cDNA, and Kirin Brewery Pharmaceutical Research Laboratory for the cytokines. We dedicate this paper for the late Prof Hisamaru Hirai, who passed away during the progress of this study.

References

1. Cumano A, Dieterlen-Lievre F, Godin I. Lymphoid potential, probed before circulation in mouse, is restricted to caudal intraembryonic splanchnopleura. Cell. 1996;86:907-916.
2. Godin IE, Garcia-Porrero JA, Coutinho A, Dieterlen-Lievre F, Marcos MA. Para-aortic splanchnopleura from early mouse embryos contains B1a cell progenitors. Nature. 1993;364:67-70.
3. Kumano K, Chiba S, Kunisato A, et al. Notch1 but not Notch2 is essential for generating hematopoietic stem cells from endothelial cells. Immunity. 2003;18:699-711.
4. Artavanis-Tsakonas S, Rand MD, Lake RJ. Notch signaling: cell fate control and signal integration in development. Science. 1999;284:770-776.
5. Okuda T, van Deursen J, Hiebert SW, Grosveld G, Downing JR. AML1, the target of multiple chromosomal translocations in human leukemia, is essential for normal fetal liver hematopoiesis. Cell. 1996;84:321-330.
6. Porcher C, Swat W, Rockwell K, Fujiwara Y, Alt FW, Orkin SH. The T cell leukemia oncoprotein SCL/tal-1 is essential for development of all hematopoietic lineages. Cell. 1996;86:47-57.
7. Tsai FY, Keller G, Kuo FC, et al. An early haematopoietic defect in mice lacking the transcription factor GATA-2. Nature. 1994;371:221-226.
8. Robert-Moreno A, Espinosa L, de la Pompa JL, Bigas A. RBPjkappa-dependent Notch function regulates Gata2 and is essential for the formation of intra-embryonic hematopoietic cells. Development. 2005;132:1117-1126.
9. Kurokawa M, Hirai H. Role of AML1/Runx1 in the pathogenesis of hematological malignancies. Cancer Sci. 2003;94:841-846.
10. Lebestky T, Jung SH, Banerjee U. A Serrate-expressing signaling center controls Drosophila hematopoiesis. Genes Dev. 2003;17:348-353.
11. Burns CE, Traver D, Mayhall E, Shepard JL, Zon LI. Hematopoietic stem cell fate is established by the Notch-Runx pathway. Genes Dev. 2005;19:2331-2342.
12. Mandal L, Banerjee U, Hartenstein V. Evidence for a fruit fly hemangioblast and similarities between lymph-gland hematopoiesis in fruit fly and mammal aorta-gonadal-mesonephros mesoderm. Nat Genet. 2004;36:1019-1023.
13. Conlon RA, Reaume AG, Rossant J. Notch1 is required for the coordinate segmentation of somites. Development. 1995;121:1533-1545.
14. Goyama S, Yamaguchi Y, Imai Y, et al. The transcriptionally active form of AML1 is required for hematopoietic rescue of the AML1-deficient embryonic para-aortic splanchnopleural (P-Sp) region. Blood. 2004;104:3558-3564.
15. Nakano T, Kodama H, Honjo T. Generation of lymphohematopoietic cells from embryonic stem cells in culture. Science. 1994;265:1098-1101.
16. Kitamura T, Koshino Y, Shibata F, et al. Retrovirus-mediated gene transfer and expression cloning: powerful tools in functional genomics. Exp Hematol. 2003;31:1007-1014.
17. Tanaka K, Tanaka T, Kurokawa M, et al. The AML1/ETO(MTG8) and AML1/Evi-1 leukemia-associated chimeric oncoproteins accumulate PEBP2beta(CBFbeta) in the nucleus more efficiently than wild-type AML1. Blood. 1998;91:1688-1699.
18. Imai Y, Kurokawa M, Yamaguchi Y, et al. The corepressor mSin3A regulates phosphorylation-induced activation, intranuclear location, and stability of AML1. Mol Cell Biol. 2004;24:1033-1043.
19. Zhang DE, Hetherington CJ, Meyers S, et al. CCAAT enhancer-binding protein (C/EBP) and AML1 (CBF alpha2) synergistically activate the macrophage colony-stimulating factor receptor promoter. Mol Cell Biol. 1996;16:1231-1240.
20. Durst KL, Hiebert SW. Role of RUNX family members in transcriptional repression and gene silencing. Oncogene. 2004;23:4220-4224.
21. Imai Y, Kurokawa M, Izutsu K, et al. Mutations of the AML1 gene in myelodysplastic syndrome and their functional implications in leukemogenesis. Blood. 2000;96:3154-3160.
22. Kageyama R, Ohtsuka T, Hatakeyama J, Ohsawa R. Roles of bHLH genes in neural stem cell differentiation. Exp Cell Res. 2005;306:343-348.
23. Kunisato A, Chiba S, Nakagami-Yamaguchi E, et al. HES-1 preserves purified hematopoietic stem cells ex vivo and accumulates side population cells in vivo. Blood. 2003;101:1777-1783.
24. Devgan V, Mammucari C, Millar SE, Brisken C, Dotto GP. p21WAF1/Cip1 is a negative transcriptional regulator of Wnt4 expression downstream of Notch1 activation. Genes Dev. 2005;19:1485-1495.
25. Kamakura S, Oishi K, Yoshimatsu T, Nakafuku M, Masuyama N, Gotoh Y. Hes binding to STAT3 mediates crosstalk between Notch and JAK-STAT signalling. Nat Cell Biol. 2004;6:547-554.
26. Stockhausen MT, Sjolund J, Axelson H. Regulation of the Notch target gene Hes-1 by TGFalpha induced Ras/MAPK signaling in human neuroblastoma cells. Exp Cell Res. 2005;310:218-228.
27. McLarren KW, Lo R, Grbavec D, Thirunavukkarasu K, Karsenty G, Stifani S. The mammalian basic helix loop helix protein HES-1 binds to and modulates the transactivating function of the runt-related factor Cbfa1. J Biol Chem. 2000;275:530-538.
28. Zamurovic N, Cappellen D, Rohner D, Susa M. Coordinated activation of notch, Wnt, and transforming growth factor-beta signaling pathways in bone morphogenic protein 2-induced osteogenesis. Notch target gene Hey1 inhibits mineralization and Runx2 transcriptional activity. J Biol Chem. 2004;279:37704-37715.
29. Garg V, Muth AN, Ransom JF, et al. Mutations in NOTCH1 cause aortic valve disease. Nature. 2005;437:270-274.
30. Yoder MC, Hiatt K, Dutt P, Mukherjee P, Bodine DM, Orlic D. Characterization of definitive lymphohematopoietic stem cells in the day 9 murine yolk sac. Immunity. 1997;7:335-344.

Research Article

Genome-Wide, High-Resolution Detection of Copy Number, Loss of Heterozygosity, and Genotypes from Formalin-Fixed, Paraffin-Embedded Tumor Tissue Using Microarrays

Sharoni Jacobs,[1] Ella R. Thompson,[2,3] Yasuhito Nannya,[4] Go Yamamoto,[4] Raji Pillai,[1] Seishi Ogawa,[5] Dione K. Bailey,[1] and Ian G. Campbell[2,3]

[1]Affymetrix, Inc., Santa Clara, California; [2]Victorian Breast Cancer Research Consortium Cancer Genetics Laboratory, Peter MacCallum Cancer Centre, East Melbourne, Victoria, Australia; [3]Department of Pathology, University of Melbourne, Parkville, Victoria, Australia; and Departments of [4]Hematology/Oncology and [5]Regeneration Medicine for Hematopoiesis, University of Tokyo, Tokyo, Japan

Abstract

Formalin-fixed, paraffin-embedded (FFPE) material tends to yield degraded DNA and is thus suboptimal for use in many downstream applications. We describe an integrated analysis of genotype, loss of heterozygosity (LOH), and copy number for DNA derived from FFPE tissues using oligonucleotide microarrays containing over 500K single nucleotide polymorphisms. A prequalifying PCR test predicted the performance of FFPE DNA on the microarrays better than age of FFPE sample. Although genotyping efficiency and reliability were reduced for FFPE DNA when compared with fresh samples, closer examination revealed methods to improve performance at the expense of variable reduction in resolution. Important steps were also identified that enable equivalent copy number and LOH profiles from paired FFPE and fresh frozen tumor samples. In conclusion, we have shown that the Mapping 500K arrays can be used with FFPE-derived samples to produce genotype, copy number, and LOH predictions, and we provide guidelines and suggestions for application of these samples to this integrated system. [Cancer Res 2007;67(6):2544–51]

Introduction

The challenges associated with DNA derived from formalin-fixed, paraffin-embedded (FFPE) samples have prevented widespread application of FFPE DNA to many of the technologies available for high-quality DNA, although some options with lower genomic coverage are available (1–3). In this study, we show the feasibility and limitations of a genome-wide assessment of genotype, loss of heterozygosity (LOH), and copy number using FFPE DNA on the Affymetrix Mapping 500K array set, which includes the Mapping 250K Nsp Array and the Mapping 250K Sty Array (Santa Clara, CA). These arrays use a process termed whole-genome sampling analysis (WGSA; ref. 4), in which genomic DNA is digested and ligated to adaptors. A subset of digested fragments are then PCR amplified in a complexity reduction step before hybridization to the arrays. PCR proved to be the critical step when processing FFPE samples.

We compared several extraction methods to determine which protocol provides FFPE DNA most suitable for array analysis and found that a PCR-based assessment of DNA quality predicted the downstream performance of FFPE DNA samples better than age of FFPE sample. We identified a necessity for (*a*) *in silico* compensation against fragment size bias and (*b*) a fragment size filter during analysis of FFPE samples. We tested our new guidelines for FFPE DNA qualification and analysis on archival samples of various tissue types, storage times, and location sources. Quality of FFPE DNA varied but the methods outlined by this study enabled prediction of performance. These results show that FFPE DNA can be suitable for a combined study of genotype, LOH, and copy number on a whole-genome scale.

Materials and Methods

Sample selection and DNA extraction. Five primary endometrioid ovarian cancers were selected without screening for the initial portion of this study. For each sample set, normal lymphocytic DNA, fresh tumor tissue, and FFPE tissue were analyzed. Samples were collected between 1993 and 1999 as part of a larger study of ovarian cancer in women living in and around Southampton, United Kingdom (5). At the time of collection, DNA was extracted from blood samples and fresh tumor biopsies were snap frozen in liquid nitrogen. A portion of each frozen tumor biopsy was sectioned to assess the proportion of tumor. For samples 526T and 594T, microdissection was done (6) to obtain DNA with a >80% tumor component. DNA was extracted from the fresh frozen tissue using a salt chloroform method (7).

In 2002, a portion of each frozen tumor biopsy was formalin fixed and paraffin embedded as described previously (8), with all tumors fixed in 10% neutral buffered formalin for <24 h at room temperature. At the time of DNA extraction, the FFPE tumors had been embedded in paraffin blocks for 3 years. Five sections (10 μm) were deparaffinized twice in xylene (5 min) and rehydrated in 100%, 90%, and 70% ethanol (1 min each). The sections were stained with hematoxylin (4 min) and washed with water (1 min), acid alcohol (10 s), water (1 min), Scott's tap water (1 min), and water (1 min). The sections were then stained with eosin (3 min), rinsed with water (10 s), and dehydrated in 70%, 90%, and 100% ethanol (30 s each). Tumor cells were manually microdissected under a dissecting microscope as described previously (6) to obtain high-purity (>80%) tumor DNA. The tumor component for sample 594 was high enough that it was not stained or microdissected. DNA was extracted from the five endometrioid FFPE tissues using a modified Qiagen protocol (Valencia, CA; described below). Following DNA extraction from FFPE tissue, a salt precipitation DNA cleanup was done as described in the Affymetrix GeneChip Mapping Assay Manuals.

For the study of independent sample sets, DNA was extracted from FFPE tissue from 17 breast tumors and 8 colorectal tumors. FFPE blocks were collected from 11 pathology laboratories and ranged in age from 1 to 17 years. The formalin fixation and paraffin embedding protocols used for these tissues are not known but are likely to be quite varied. For breast

---

Note: Supplementary data for this article are available at Cancer Research Online (http://cancerres.aacrjournals.org/).

S. Jacobs and E.R. Thompson contributed equally to this work.

Conflict of Interest Statement: S. Jacobs, R. Pillai, and D.K. Bailey are employees of Affymetrix, Inc.

Requests for reprints: Sharoni Jacobs, Affymetrix, Inc., 3420 Central Expressway, Santa Clara, CA 95051. Phone: 408-731-5880; Fax: 408-481-0435; E-mail: sharoni_jacobs@affymetrix.com.

doi:10.1158/0008-5472.CAN-06-3597

tumors, 10 μm sections were deparaffinized, stained with H&E, and manually microdissected (described above). The colorectal tumors were not stained or microdissected due to their high tumor component. DNA was extracted from breast and colorectal tissues (described below), and as before, a salt precipitation DNA cleanup was done.

The collection and use of tissues for this study were approved by the appropriate institutional ethics committees.

Trial of DNA extraction methods for FFPE tissue. Five DNA extraction methods were trialed using whole 20 μm sections from three FFPE blocks. The methods that were compared were the MagneSil Genomic Fixed Tissue System (Promega,[6] Madison, WI), ChargeSwitch gDNA Micro Tissue kit (Invitrogen,[7] Carlsbad, CA), PureGene (Gentra Systems,[8] Minneapolis, MN), DNeasy Tissue kit (Qiagen[9]), and a phenol/chloroform extraction. With the exception of the DNeasy Tissue kit and phenol/chloroform, the extractions were done according to the manufacturer's instructions. The extractions done with the DNeasy Tissue kit and with phenol/chloroform both were modified to include an initial incubation at 95°C for 15 min followed by 5 min at room temperature as described previously (9), before being digested with proteinase K for 3 days at 56°C in a rotating oven with periodic mixing and fresh enzyme added each 24 h. A salt precipitation was done on DNA from all five extraction methods.

DNA quality assessment and preparation. The extracted DNA was quantified using UV spectroscopy at 260 nm. Random amplified polymorphic DNA-PCR (RAPD-PCR; ref. 10) was done to assess the quality of DNA and maximum fragment lengths as described previously using 50, 5, or 0.5 ng DNA (11). Qiagen HotStarTaq was used, with 0.4 units per reactions (Qiagen[9]). Products were visualized with ethidium bromide on a 3% gel.

Preparation and application of DNA to the mapping arrays. Matched fresh and FFPE samples were analyzed on the Affymetrix GeneChip Human Mapping 10K v2 Xba Array and 50K Xba Array and prepared using the Mapping 10K v2 Assay kit and the Mapping 100K Assay kit (Affymetrix)[10] The only exception to the manufacturer's protocol was that 10 cycles were added to the PCR cycling conditions for each FFPE sample.

Matched fresh tumor, FFPE tumor, and normal samples were assayed using the Mapping 250K Nsp Assay kit and the Mapping 250K Sty Assay kit[10] and hybridized to the 250K arrays. The 500K assay was done according to the manufacturer's protocol, beginning with 250 ng DNA. Ninety micrograms of PCR product were fragmented and labeled, using additional PCRs when necessary for FFPE breast and colorectal samples.

Data analysis. Genotype calls were produced using the dynamic model algorithm (12) by the Affymetrix GeneChip Genotyping Analysis Software version 4.0. A stringent P value cutoff threshold of 0.26 was used. Concordance was determined by calculating the number of single nucleotide polymorphisms (SNP) that gave the same call in both fresh frozen and FFPE DNA from the same tumor and dividing this number by the total number of SNPs that were called in both samples.

LOH predictions were produced using dChipSNP software (dChip2005_f4 version[11]; ref. 13). LOH values were inferred using the Hidden Markov Model and restricting to SNPs on fragment sizes ≤700 bp.

Copy number estimates for ovarian tumor samples using 500K data were determined by pairing tumor and matching normal samples in CNAG_v2.0.[12] Nonpaired, nonmatching references were used for copy number prediction of 10K and 50K data. Log 2 ratios were imported into Spotfire DecisionSite (Spotfire,[13] Somerville, MA) and the Affymetrix Integrated Genome Browser for visualization and comparison. Copy number estimates for breast and colon FFPE tumors were done using data from 48 HapMap samples (available online[10]) as a reference.

Estimated inter-SNP mean and median distances after exclusion of fragment sizes >700 bp were determined by first calculating the distance between all SNPs on each chromosome. Distances were then sorted per chromosome in descending order and the largest distances (representing centromeres) were removed for each chromosome, except for the acrocentric chromosomes 13 to 15 and 21 to 22.

Pearson (linear) correlations were calculated in Partek Genomics Suite (Partek,[14] St. Louis, MO).

Microsatellite analysis. Nine microsatellite markers were used to assess LOH at three loci: chromosome 1q (D1S2816, D1S413, and D1S1726), chromosome 7p (D7S691, D7S670, and D7S2506), and chromosome 14q (D14S1011, D14S258, and D14S1002). Regions were selected where array-based LOH analysis showed discordant LOH results for fresh and FFPE-derived DNA. The forward primer was labeled with a 5′-fluorescent dye (FAM or HEX). The samples were analyzed using a 3130 Genetic Analyzer (Applied Biosystems,[15] Foster City, CA) with POP7 polymer. An assessment of LOH was done using GeneMapper version 3.7. LOH was scored by calculation of the ratio of tumor DNA peaks (T1/T2) compared with that in the normal DNA to give a relative ratio (T1/T2)/(N1/N2). A ratio of 0 indicates complete allele loss and a ratio of 1 indicates no LOH. A ratio of <0.5 was scored as indicative of LOH.

Results

DNA extraction from FFPE tissue. Five DNA extraction methods (phenol/chloroform, Qiagen DNeasy Tissue kit, Invitrogen ChargeSwitch, Promega MagneSil, and Gentra PureGene) were tested on consecutive sections from different FFPE ovarian tumor biopsies. Phenol/chloroform and modified Qiagen protocols (see Materials and Methods) provided the highest DNA yield as determined by UV spectroscopy; these yields were 2.2 times more than the average yield from any of the other three extraction protocols (Fig. 1*A*). RAPD-PCR, which uses primers of 10 bps to produce a ladder of amplicons, was also done to assess both amplification efficiency and maximum product size for each extraction protocol (11). Compared with DNA extracted from fresh lymphocytes, the FFPE-derived DNA from all extraction methods yielded consistently smaller PCR fragments, with a maximum reliable size of ~800 bp (Fig. 1*A*). Phenol/chloroform and modified Qiagen extractions produced more intense and consistent PCR fragments across dilutions, suggesting that products were relatively free of contaminant inhibitors (Fig. 1*A*). DNA extracted with these two methods was processed through the PCR step of the Mapping 50K Xba Assay to further assess amplification efficiency. In this test, the modified Qiagen extraction provided a slightly higher PCR yield on average than the phenol/chloroform method (21.4 μg compared with 19.2 μg) and was therefore chosen for DNA extraction from FFPE tissues in this study.

Mapping 500K array performance. Five matched sets; each containing (*a*) nontumor, non-FFPE lymphocytic DNA, (*b*) fresh frozen ovarian tumor DNA, and (*c*) FFPE ovarian tumor DNA; were assessed for performance on the Mapping 500K arrays. All five FFPE samples had been stored for 3 years and provided average RAPD-PCR maximum amplicon sizes from 526 to 800 bp. During the PCR step of the Mapping assay, amplification products from all five FFPE tumors were concentrated <700 bp, a fragment size range that was reduced compared with non-FFPE samples (Fig. 1*B*). Decreased yield from the Mapping PCRs (Table 1) accompanied the decrease in amplicon size distributions. FFPE samples produced

[6] http://www.promega.com
[7] http://www.invitrogen.com
[8] http://www.gentra.com
[9] http://www.qiagen.com
[10] http://www.affymetrix.com
[11] http://www.dchip.org
[12] http://www.genome.umin.jp/
[13] http://www.spotfire.com
[14] http://www.partek.com
[15] http://www.appliedbiosystems.com

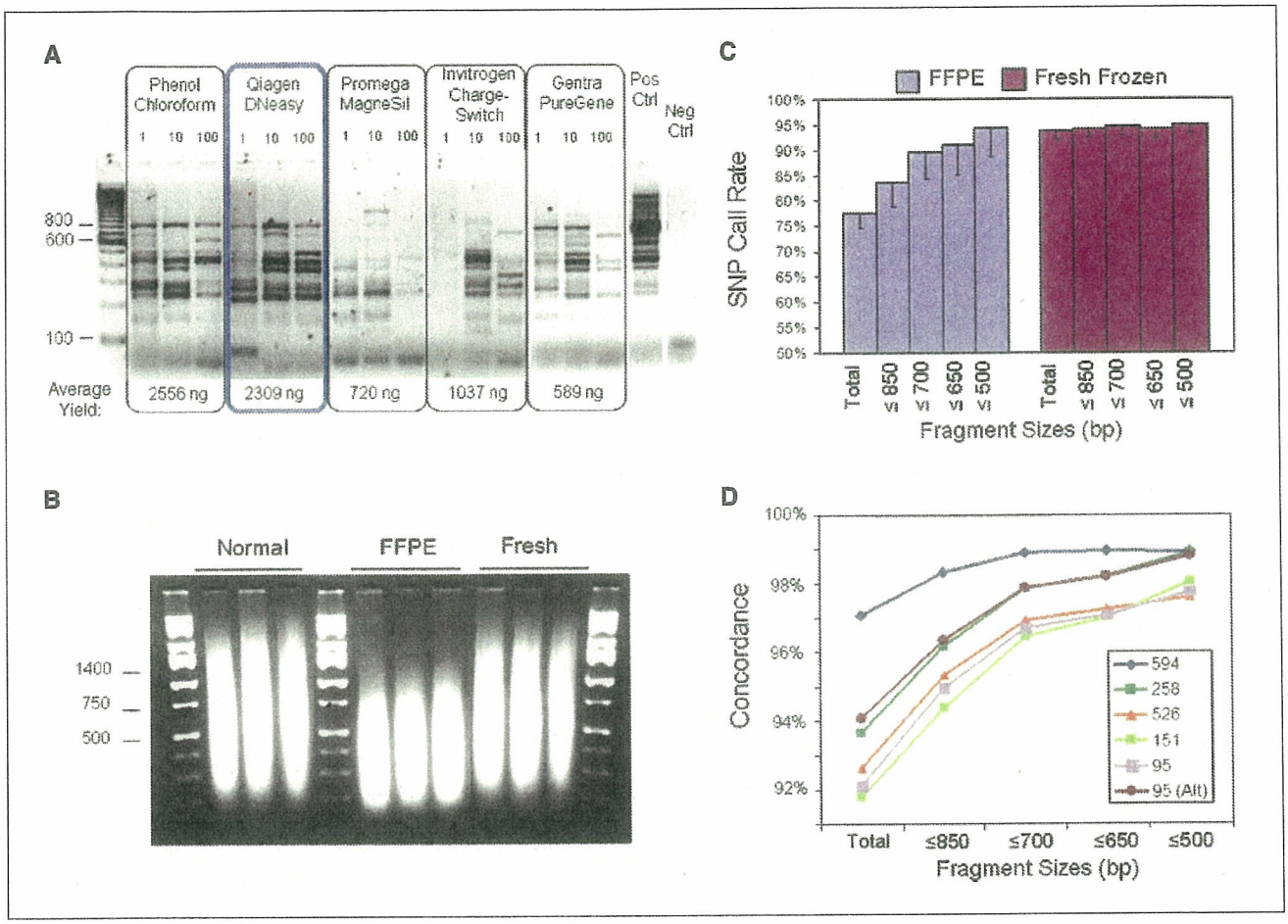

Figure 1. Performance of different FFPE DNA extraction methods and the Affymetrix GeneChip Mapping 500K assay. *A,* visualization of RAPD-PCR products on a 3% agarose gel comparing the undiluted DNA extraction (1), a 1:10 dilution of input DNA (10), and a 1:100 dilution of DNA (100) from one FFPE tissue (047) using five different extraction methods. The maximum fragment size in the extracted FFPE DNA samples reached 1,100 bp although only with sample dilution. The maximum reproducible fragment was 800 bp. DNA yield per extraction method is listed below. *B,* visualization of the PCR products during the Mapping 500K assay reveals a downshift in the distribution of fragment size, which is specific to the FFPE samples. *C,* SNP call rates are reduced in FFPE samples, but SNPs on smaller fragments are genotyped with equal efficiency from fresh and paraffin samples. The size dependence for higher call rates is specific to the FFPE samples. *D,* concordance between fresh frozen and matching FFPE samples is incrementally increased with fragment size selectivity, with larger dips in accuracy for sizes >700 bp. Exclusion of some regions (chromosomes 1q, 7p, 15, and 16q) shown to be genetically different between 95 fresh and FFPE samples causes an upshift in concordance for this sample (95 Alt versus 95).

63 to 83 μg PCR products for the Mapping 250K Nsp Array, whereas all non-FFPE samples produced >90 μg.

The assay was continued using 90 μg PCR product as the manual instructs or the total PCR yield when this was less than assay requirements. Importantly, the protocol was otherwise never modified. Normal and fresh tumor samples gave typical SNP call rates, with an average of 94.5% and 93.5%, respectively. These call rates are lowered due to application of a strict confidence score threshold ($P \leq 0.26$; the default threshold is $P \leq 0.33$). In contrast, FFPE samples achieved an overall average call rate of 79.84% and 75.17% for Nsp and Sty, respectively (Table 1). These decreased call rates are consistent with the poor amplification of larger fragments during PCR. Exclusion of SNPs on larger fragments significantly increased the call rates, such that incrementally more stringent fragment size restrictions incrementally increased call rates (Fig. 1*C*). In fact, stringent fragment size restrictions produced similar call rates between fresh frozen and FFPE samples, indicating that the Mapping 500K is well suited for FFPE DNA and identifying the limiting factor as the size of amplicons produced from the degraded DNA.

Concordance of genotype calls between paired FFPE and fresh frozen ovarian tumor DNA samples was examined to determine the reliability of genotypes from FFPE DNA. It is important to note that tumor heterogeneity lead to confirmed genuine differences in genomic content between matched FFPE and fresh frozen DNA, which would lower these concordance rates. Average overall concordance between FFPE and fresh frozen samples from the same tumor was 93.6%. Exclusion of the larger fragments increased concordance such that all SNPs located on fragment sizes ≤700 bp displayed an average of 97.4% concordance (Fig. 1*D*). Exclusion of several regions (chromosomes 1q, 7p, 15, and 16q) displaying heterogeneity between fresh frozen and paraffin sample 95 increased the concordance by >2% (Fig. 1*D*). These high rates of concordance, despite shown genetic differences between paired samples, underscore the reliability and reproducibility of genotype calls produced using FFPE-derived DNA samples with this

Table 1. Performance of normal, fresh frozen, and FFPE samples on Affymetrix GeneChip Mapping 10K v2, 50K Xba, 250K Nsp, and 250K Sty arrays

Type	Array	PCR yield* (μg)	Call rate† (%)	AA call (%)	AB call (%)	BB call (%)	Signal detection‡ (%)	MCR§ (%)	MDR‖ (%)	Overall concordance¶ (%)
Fresh tumor	10K v2	20.4	93.44	37.96	23.50	38.54	99.82	—	—	96.20
FFPE tumor	10K v2	19.2	86.30	39.77	19.83	40.41	97.39	—	—	
Fresh tumor	50K Xba	48.3	90.07	40.28	20.24	39.48	—	87.65	98.57	56.95
FFPE tumor	50K Xba	46.0	31.86	47.30	6.76	45.94	—	15.25	22.15	
Normal	250K Nsp	115.1	95.86	37.95	25.54	36.51	—	94.22	98.60	
Fresh tumor	250K Nsp	114.4	93.99	41.81	18.09	40.10	—	88.26	98.52	94.74
FFPE tumor	250K Nsp	71.6	79.84	43.42	14.89	41.69	—	65.60	80.32	
Normal	250K Sty	121.1	93.05	38.87	24.28	36.85	—	90.90	97.45	
Fresh tumor	250K Sty	114.4	92.96	42.38	17.59	40.03	—	87.95	98.38	92.07
FFPE tumor	250K Sty	95.4	75.17	43.66	16.68	39.66	—	62.57	79.37	

*For the 250K arrays, this is the total yield of DNA obtained after combining three PCRs according to protocol. For the 10K v2 and 50K arrays, the PCR yield for the FFPE tissues was increased by increasing either the number of reactions or the number of PCR cycles.
† Percentage of SNPs able to be genotyped.
‡ Signal detection used to assess 10K arrays.
§Modified partitioning around medoids (MPAM; a genotyping algorithm; ref. 17) call rate used to assess 100K and 500K arrays.
‖MPAM detection rate used to assess 100K and 500K arrays.
¶Percentage of SNPs genotyped in both fresh frozen and FFPE samples that are given the same genotype.

platform. Importantly, it indicates the need to exclude SNPs on larger fragments for reliable genotype data. Because SNP fragment size is distributed randomly across the genome, the general effect of excluding larger fragment sizes is to reduce the overall resolution without preferentially losing extensive coverage in specific regions (see Supplementary Fig. S1). The effect of fragment size on concordance was specific to FFPE samples and is not observed in comparisons between frozen samples (data not shown).

LOH and copy number assessment. The reliability of genotype assignments using paraffin samples suggests their suitability for LOH predictions. In fact, FFPE and fresh tumor pairs produced similar LOH profiles when including SNPs on fragments sizes ≤700 bp (Fig. 2*A*). Regions of inconsistent LOH predictions between paired samples (for example, see Fig. 2*A, boxes*) were predicted independently by both Nsp and Sty arrays and appeared along concentrated regions, rather than being sporadically distributed across the genome, suggesting that they reflected true biological differences between the samples. We assessed several discordant regions of LOH using conventional microsatellite marker analysis and in all cases, the microsatellite analysis confirmed that the array predictions were genuine (data not shown).

The ability to associate copy number estimates with SNP genotypes relies on quantitation of SNP probe intensities (14). Because larger fragment SNPs were inadequately amplified during WGSA, these SNPs were noninformative for copy number analysis of FFPE samples (Supplementary Fig. S2A). Exclusion of these large fragment SNPs significantly increased the amplitude (signal) of copy number shifts and at the same time reduced the SD (noise) associated with the copy number estimates for all FFPE samples but not the fresh frozen samples (Supplementary Fig. S2B). This increase in signal to noise ratio justifies the use of such a filter, which maintained 308,788 SNPs for FFPE copy number analysis (Table 2). Probe intensities from the remaining smaller fragment SNPs predicted copy number profiles for FFPE samples consistent with those from matching fresh frozen material (Fig. 2*B*). Equivalent copy number changes were predicted between FFPE and fresh frozen pairs both across different chromosomes and different sample sets (Fig. 2*C*).

In addition to limiting fragment size, compensation against fragment size bias was necessary to produce reliable copy number predictions. Although bias due to amplicon size can be negligible when using high-quality DNA, it becomes exaggerated when the DNA sample is degraded (Fig. 3, *top*). For FFPE samples, the mean copy number was grossly affected by the size of the amplicon carrying the SNP, such that smaller amplicons SNPs predicted gains and larger amplicons SNPs predicted losses in copy number. Quadratic regression helped to neutralize this fluctuation in mean copy number (Fig. 3, *middle*). Exclusion of SNPs on amplicons >700 bp before regression effectively removed the fragment size bias from copy number detection (Fig. 3, *bottom*). Copy number analysis of FFPE samples was done using the freely available CNAG_v2.0 software[12] (15), which automatically uses compensation against fragment size bias and includes an option to exclude SNPs based on fragment size. Alternate software tools that lack this compensation produced copy number estimates from FFPE samples that were noisier even with exclusion of large fragment sizes (data not shown).

Comparison of Mapping 10K, 100K, and 500K array performance. Although the various Mapping arrays all use the same technology and similar assays for genotype and copy number analysis, they each have differences that may influence their compatibility with FFPE samples. Particularly, the Mapping 500K and 10K arrays share the same amplicon distribution during the PCR step of WGSA, but the Mapping 100K assay relies on a wider amplicon size distribution (250–2,000 bp). Consequently, Mapping 100K data are more significantly affected by DNA degradation; for example, there are only 59 SNPs on fragment sizes <500 bp on the Mapping 50K Hind array. Previously, we showed the application of FFPE DNA to the 10K arrays (3) although without the analytic tools applied here. Now, we compared performance of FFPE samples on all Mapping arrays. As expected, call rates and concordances were

poor when FFPE DNA was applied to the Mapping 100K assay, whereas performance was similar for the Mapping 500K and 10K arrays (Table 1; Supplementary Fig. S3). Furthermore, both the Mapping 500K and the 10K arrays, but not the Mapping 100K arrays, provided correct copy number predictions from FFPE DNA, whereas the Mapping 500K arrays best accommodated SNP filters to retain high genomic resolution (Supplementary Fig. S3).

Prediction of mapping array performance for a range of FFPE samples. DNA from FFPE samples can vary in quality as a result of the fixation protocol, years of storage, the extraction protocol, tissue source, and several other uncontrollable and controllable variables. To both identify a method for qualifying FFPE DNA samples for array analysis and test our guidelines for FFPE DNA extraction and data analysis, we measured the performance of an additional 25 FFPE tissue sources processed at separate institutes and stored for 1 to 17 years (Supplementary Table S1). These samples were not prescreened nor selected based on expected performance. Experiments were done without matched fresh frozen or nontumor samples. In a small test set, we found that application of 90 μg PCR product from FFPE samples increased call rates by several percentage points (data not shown); therefore, we assayed these samples using 90 μg whenever possible, even if this required pooling extra PCRs.

For each sample, we noted the largest amplicon size produced during RAPD-PCR as well as the size range of PCR products during the Mapping assay. Call rates were calculated for SNPs on fragment size ≤200 bp, 250 bp, 300 bp, and so on to determine the size at which call rates dropped <90%. This call rate drop-off value was used to indicate genotyping efficiency and reliability because fragment sizes with high call rates provided high concordance as well. Call rate drop-off values ranged from 250 to 750 bp compared with 700 to 850 bp for the five FFPE ovarian tumors. Therefore, most of these samples would provide reduced resolution for genotype and LOH. Copy number detection was more robust than genotype, and those cutoffs ranged from 300 bp up to no filter requirement at all. Plots of copy number versus fragment size were evaluated to

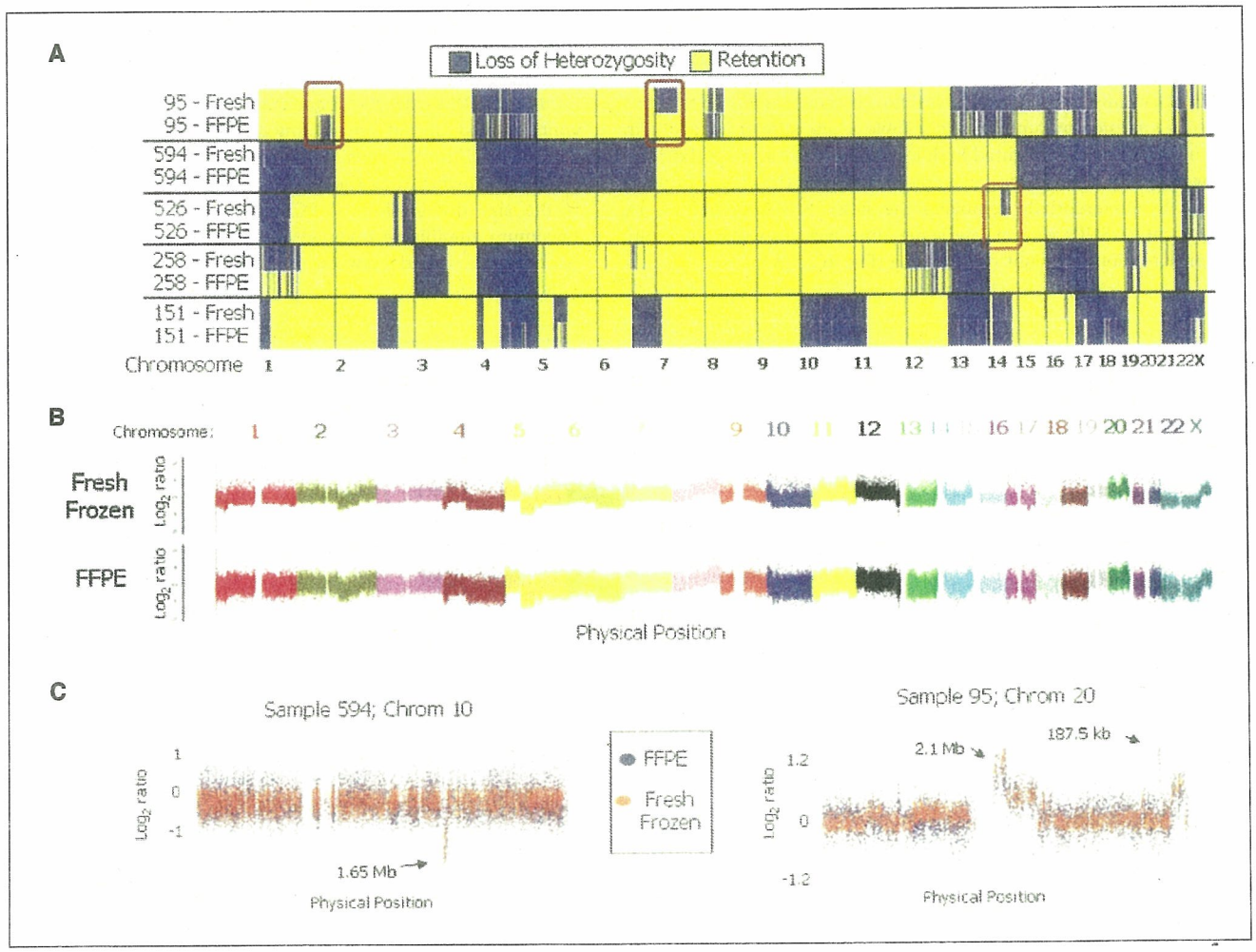

Figure 2. Genome-wide plots of LOH and copy number for fresh frozen and FFPE samples. *A,* genome-wide display of inferred LOH for fresh frozen and FFPE samples, including SNPs on fragments sizes ≤700 bp. *Blue regions,* LOH; *yellow regions,* retention of heterozygosity. Chromosome numbers are indicated below. Three discordant LOH predictions specific to either fresh frozen or FFPE samples were confirmed by microsatellite analysis of DNA (*brown boxes*, regions). *B,* raw single SNP log 2 ratios indicate gains and losses for fresh frozen (above) and FFPE (below) sources of sample 151 across the genome. Ratios represent copy number of tumor DNA over copy number of nontumor, non-FFPE lymphocytic DNA. Each color represents a different chromosome. SNPs were filtered for fragments ≤700 bp for the FFPE sample. *C,* raw single SNP log 2 ratios for fresh frozen (*orange*) and FFPE (*blue*) DNA are plotted across single chromosomes of multiple samples. SNPs were filtered for fragments ≤700 bp for FFPE data only. Highlighted copy number changes were confirmed by quantitative PCR.

Table 2. SNP numbers per fragment size filters

Fragment sizes included (bp)	250K Nsp array	250K Sty array	500K array set
≤300	13,636	15,845	29,481
≤400	39,492	45,473	84,965
≤500	74,372	82,099	156,471
≤600	113,687	120,025	233,712
≤650	133,748	138,282	272,030
≤700	153,198	155,590	308,788
≤800	190,899	187,687	378,586
≤850	209,017	201,004	410,021
≤900	222,316	213,300	435,616
≤1,000	244,644	230,527	475,171
Total	262,256	238,300	500,568

determine the optimal fragment size filter for copy number analysis. These plots can be viewed in CNAG_v2.0, and various fragment size filters can be applied until the mean copy number for the SNPs retained in analysis are consistent across fragment size (Fig. 4*C*, *left*). An example of this entire workflow is shown in Fig. 4*A* to *C* and results are listed in Supplementary Table S1. As shown for a 733-kb hemizygous loss highlighted in this example, the fragment size filter suggested by this process was able to increase the signal to noise ratio by preferentially removing the noisy SNPs instead of the informative SNPs and at the same time was also able to retain higher resolution by not overfiltering (Fig. 4*C*, *right*).

Years of storage and overall call rates displayed some correlation to copy number and call rate drop-off values, but PCR-based analyses had higher predictive power for these performance metrics (Fig. 4*D*). The Pearson's correlation of median RAPD-PCR values to copy number drop-off was 0.93, indicating high predictive power. Comparison of array performance to PCR-based DNA quality tests gave R^2 values above 0.8. In contrast, R^2 values were <0.7 when comparing performance with years of storage or comparing copy number drop-off with overall call rate. These results indicate that a PCR-based test of DNA quality is a reasonable method for predicting whether a FFPE DNA sample will be amenable to array analysis.

Six of the 25 samples (two breast and four colorectal) were not applied to the arrays because no RAPD-PCR products were produced. Sample 0588 also failed RAPD-PCR, but it was still applied to the array. Consistent with the RAPD-PCR prediction, this sample was the only example, in which call rates broken up by fragment size never exceeded 90%, and data from even the smallest fragment SNPs were too noisy for copy number analysis.

Discussion

There exists a large and growing deposit of archived clinical tissues, yet DNA extracted from these samples is usually degraded, contaminated, and of general low quality. This study expands the usefulness of the Mapping 500K arrays to DNA derived from FFPE samples, showing that the limiting factor for FFPE application is the size distribution of PCR amplicons during WGSA. The maximum amplifiable fragment size, which is correlated to array performance, varied between samples and may be influenced by

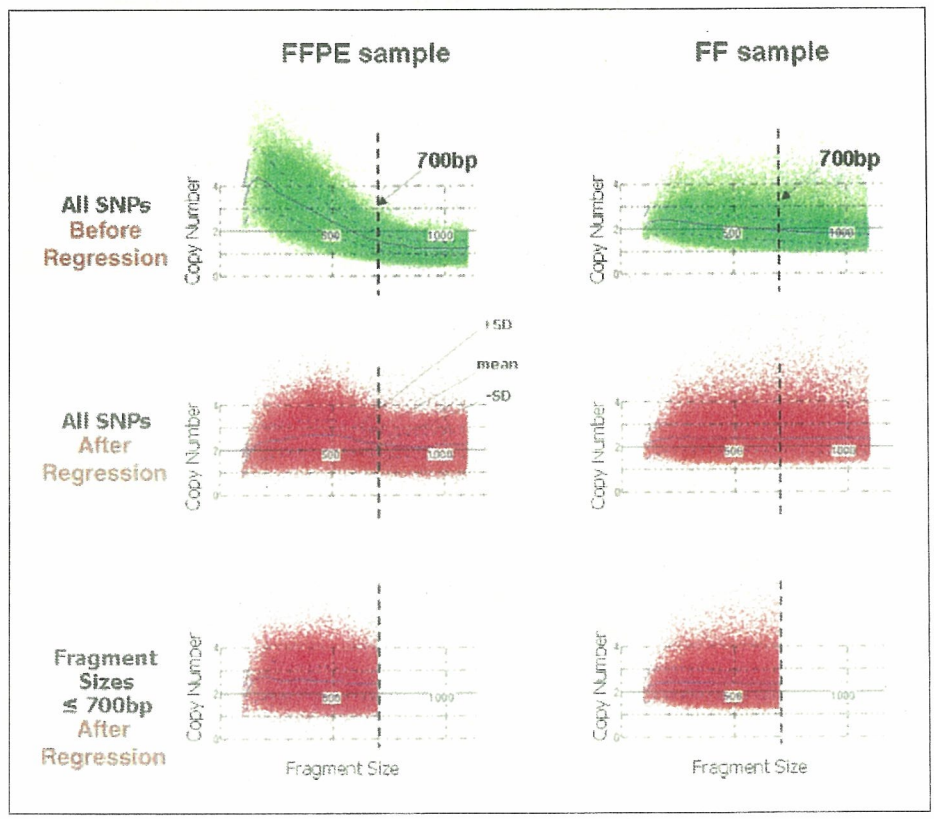

Figure 3. Compensation against fragment size bias enables effective copy number analysis of FFPE samples. Raw predicted copy number (*Y-axes*) is influenced by fragment size (*X-axes*) in fresh frozen (*right*) and FFPE (*left*) samples, although the effect is exaggerated in the latter (see *blue solid lines, middle*). This causes an overestimate of copy number for fragments below ~500 bp and an underestimate for those above ~500 bp. Compensation against fragment size corrects this bias such that the mean predicted copy number (*blue line*) is constant independent of fragment size in fresh frozen samples (*bottom right*). For FFPE samples, exclusion of noninformative larger fragments before quadratic regression is required to effectively equilibrate copy number across maintained SNPs (*top left*).

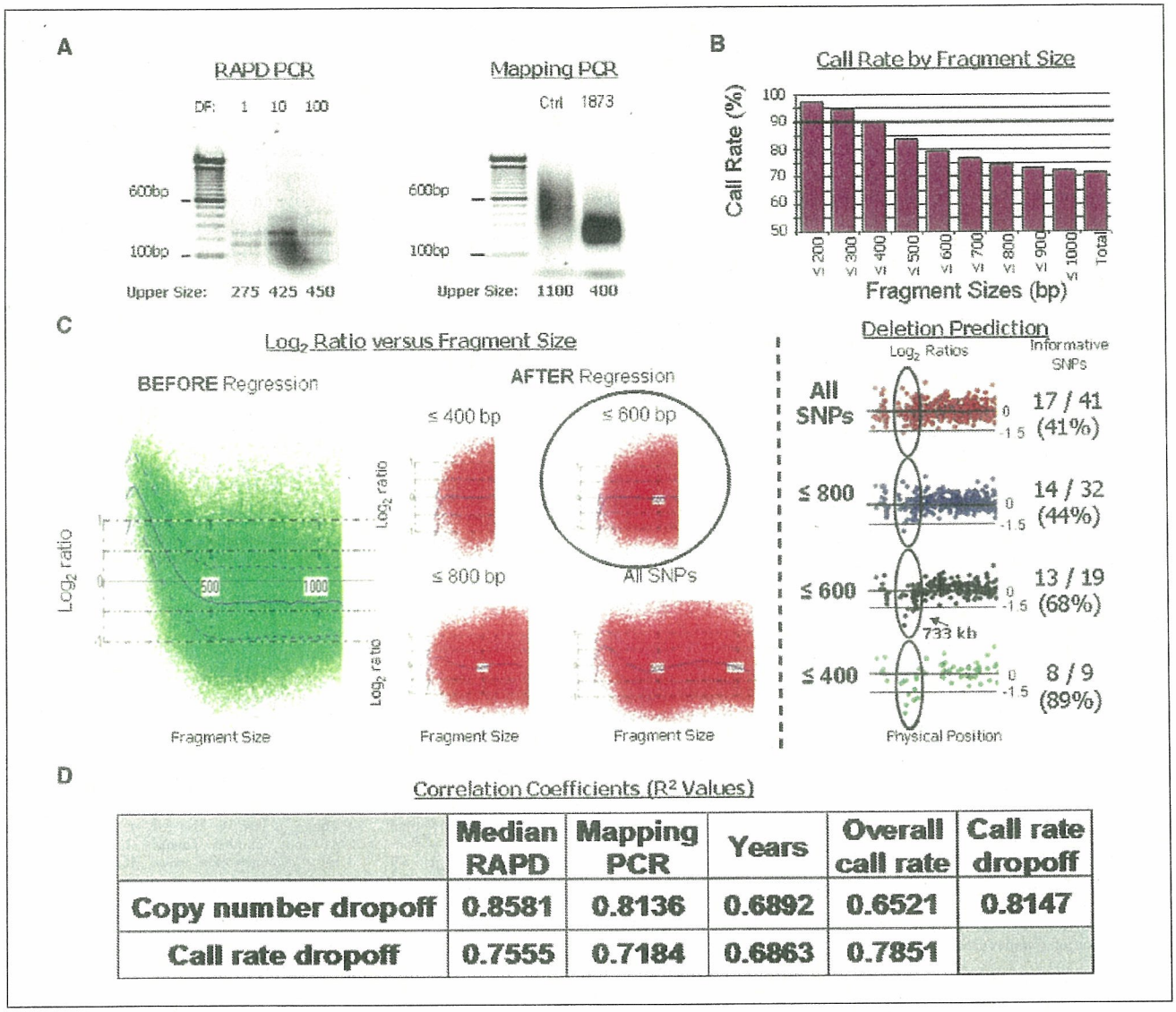

	Median RAPD	Mapping PCR	Years	Overall call rate	Call rate dropoff
Copy number dropoff	0.8581	0.8136	0.6892	0.6521	0.8147
Call rate dropoff	0.7555	0.7184	0.6863	0.7851	

Figure 4. Prediction of FFPE sample performance. *A,* display of RAPD-PCR and Mapping assay PCR for a single breast tumor sample (1873). Maximum size amplicons from RAPD-PCR varied from 275 to 450 bp, with dilution factors (*DF*) of 1, 10, and 100. Although high-quality DNA had a maximum upper fragment size of ~1,100 after PCR during the Mapping assay, this sample was well amplified only up to ~400 bp. *B,* call rate by fragment size was monitored for the same sample, using a stringent confidence value threshold of 0.26. Call rates dropped <90% when excluding SNPs on fragment sizes >400 bp. *C,* copy number versus fragment size plots in CNAG_v2.0 show a strong influence by fragment size on copy number predictions before correction (*left*). Regression corrects this bias somewhat, and more and more stringent filters further correct this bias (*middle*). With a filter excluding SNPs on fragment sizes >600 bp, the mean copy number (*blue line*) is consistent regardless of fragment size, indicating that this sample requires a copy number filter at 600 bp. Log 2 ratios produced using various fragment size filters are displayed for a region containing a 733-kb deletion on part of chromosome X. Under "Informative SNPs," the number of SNPs predicting a deletion with a log 2 ratio below −0.3 (considered to be "informative") are listed to the left of the number of total SNPs within the deletion region that were retained during the fragment size filter. Below these values is the percentage of SNPs included in the analysis that were informative of the deletion. *D,* R^2 regression values when the fragment size at which call rates drop <90% or the maximum fragment size that can be included in copy number analyses are compared with median maximum RAPD-PCR amplicon size, maximum Mapping PCR amplicon size, years of storage, or overall call rate ($P \leq 0.26$) are displayed. PCR tests better predicted copy number performance than years of storage or overall call rate, and they were better predictors of genotype performance than years of storage was.

both extent of DNA degradation and modification as well as the amount of inhibitors remaining in the sample. Use of a suitable DNA extraction protocol, such as the DNeasy Tissue kit, is important for obtaining DNA amenable to the assay, but other factors, such as years of storage and fixation process, will be harder to control. This underscores the necessity for a pre-WGSA quality control step that includes PCR of larger fragment sizes, such as RAPD-PCR or multiplex PCR (16). This study attempts to outline guidelines for qualifying FFPE DNA samples and analyzing qualified samples, but not all FFPE blocks will yield DNA suitable for the Mapping arrays.

FFPE DNA that is applied to the arrays may still vary in quality and therefore require more or less stringent fragment size filters. Despite reduction in coverage to accommodate loss of larger fragments, high resolution for genotype, LOH, and copy number assessment can still be maintained (Table 2; Supplementary Fig. S1). This is true because of the large number of SNPs on small fragments and because fragment size seems to be the only limiting

factor. For example, with exclusion of SNPs on amplicons >700 bp, as was required for the first set of five FFPE samples, 308,788 SNPs were retained for analysis, providing a median and mean inter-SNP distance of 4.3 or 9.5 kb, respectively. Although the 10K array is also suitable for analysis of degraded DNA (3), the large SNP coverage and the small fragment emphasis of the Mapping 500K arrays make it ideal for FFPE sample analysis.

The percentage of FFPE samples archived in banks that could be applied to the arrays with limited loss in genomic resolution would be influenced by the methods of fixation and extraction used at various institutes. Importantly, all samples stored for 6 years or fewer provided copy number data for a minimum of 234K SNPs in this study. Some of the samples applied to the arrays required extremely stringent filters against fragment size, resulting in significantly decreased resolution of genomic data. Potentially, researchers may choose only to analyze DNA samples of such low quality when the FFPE sample is considered to be particularly precious. Importantly, RAPD-PCR results predicted that these samples would display decreased performance on the array and a PCR screen could be applied to avoid application of poorly doing samples. With the advent of more standardized protocols for sample processing in the future and with advances in DNA extraction, a higher proportion of FFPE samples may be applicable to the arrays.

Despite the large banks of FFPE samples available for retrospective studies that include follow-up analysis of patient outcome, most of these studies currently focus on frozen samples because of the limited options available for paraffin samples. Additionally, FFPE processing holds advantages for tissue storage during prospective studies, in which many biopsies are collected but only a fraction of them are applied to downstream assays with selection based on clinical outcome. These results outline guidelines for the application of FFPE samples to the same genome-wide platform already available to high-quality DNA samples, thus enabling widespread retrospective and prospective analysis of tumor samples in their most common form of storage.

Acknowledgments

Received 10/2/2006; revised 12/19/2006; accepted 1/8/2007.

Grant support: National Breast Cancer Foundation postgraduate research scholarship (E.R. Thompson).

The costs of publication of this article were defrayed in part by the payment of page charges. This article must therefore be hereby marked *advertisement* in accordance with 18 U.S.C. Section 1734 solely to indicate this fact.

We would like to thank Giulia Kennedy, Manqiu Cao, Yaron Turpaz, and Guoliang Xing for technical input and discussions, Michael Shapero for his helpful suggestions and critical reading of the manuscript, and Dr. Alex Dobrovic for his help with DNA extraction.

References

1. Wang Y, Moorhead M, Karlin-Neumann G, et al. Allele quantification using molecular inversion probes (MIP). Nucleic Acids Res 2005;33:e183.
2. Lips EH, Dierssen JW, van Eijk R, et al. Reliable high-throughput genotyping and loss-of-heterozygosity detection in formalin-fixed, paraffin-embedded tumors using single nucleotide polymorphism arrays. Cancer Res 2005;65:10188–91.
3. Thompson ER, Herbert SC, Forrest SM, Campbell IG. Whole genome SNP arrays using DNA derived from formalin-fixed, paraffin-embedded ovarian tumor tissue. Hum Mutat 2005;26:384–9.
4. Kennedy GC, Matsuzaki H, Dong S, et al. Large-scale genotyping of complex DNA. Nat Biotechnol 2003;21:1233–7.
5. Bryan EJ, Watson RH, Davis M, Hitchcock A, Foulkes WD, Campbell IG. Localization of an ovarian cancer tumor suppressor gene to a 0.5-cM region between D22S284 and CYP2D, on chromosome 22q. Cancer Res 1996;56:719–21.
6. Jiang X, Hitchcock A, Bryan EJ, et al. Microsatellite analysis of endometriosis reveals loss of heterozygosity at candidate ovarian tumor suppressor gene loci. Cancer Res 1996;56:3534–9.
7. Mullenbach R, Lagoda PJL, Welter C. An efficient salt chloroform extraction of DNA from blood and tissues. Trends Genet 1989;5:391.
8. Bancroft JD, Stevens A. Theory and practice of histological techniques. 3rd ed. London: Churchill Livingstone; 1991. p. 48–57.
9. Wu L, Patten N, Yamashiro CT, Chui B. Extraction and amplification of DNA from formalin-fixed, paraffin-embedded tissues. Appl Immunohistochem Mol Morphol 2002;10:269–74.
10. Williams JG, Kubelik AR, Livak KJ, Rafalski JA, Tingey SV. DNA polymorphisms amplified by arbitrary primers are useful as genetic markers. Nucleic Acids Res 1990;18:6531–5.
11. Siwoski A, Ishkanian A, Garnis C, Zhang L, Rosin M, Lam WL. An efficient method for the assessment of DNA quality of archival microdissected specimens. Mod Pathol 2002;15:889–92.
12. Di X, Matsuzaki H, Webster TA, et al. Dynamic model based algorithms for screening and genotyping over 100 K SNPs on oligonucleotide microarrays. Bioinformatics 2005;21:1958–63.
13. Lin M, Wei LJ, Sellers WR, Lieberfarb M, Wong WH, Li C. dChipSNP: significance curve and clustering of SNP-array-based loss-of-heterozygosity data. Bioinformatics 2004;20:1233–40.
14. Huang J, Wei W, Zhang J, et al. Whole genome DNA copy number changes identified by high density oligonucleotide arrays. Hum Genomics 2004;1:287–99.
15. Nannya Y, Sanada M, Nakazaki K, et al. A robust algorithm for copy number detection using high-density oligonucleotide single nucleotide polymorphism genotyping arrays. Cancer Res 2005;65:6071–9.
16. van Beers EH, Joosse SA, Ligtenberg MJ, et al. A multiplex PCR predictor for aCGH success of FFPE samples. Br J Cancer 2006;94:333–7.
17. Liu WM, Di X, Yang G, et al. Algorithms for large-scale genotyping microarrays. Bioinformatics 2003;19:2397–403.